Prediction of Tornado-Like Vortex (TLV) Embedded in the 8 May 2003 Oklahoma City Tornadic Supercell Initialized from the Subkilometer Grid Spacing Analysis Produced by the Dual-Resolution GSI-Based EnVar Data Assimilation System

YONGMING WANG AND XUGUANG WANG

School of Meteorology, University of Oklahoma, Norman, Oklahoma

ABSTRACT

Explicit forecasts of a tornado-like vortex (TLV) require subkilometer grid spacing because of their small size. Most previous TLV prediction studies started from interpolated kilometer grid spacing initial conditions (ICs) rather than subkilometer grid spacing ICs. The tornadoes embedded in the 8 May 2003 Oklahoma City tornadic supercell are used to understand the impact of IC resolution on TLV predictions. Two ICs at 500-m and 2-km grid spacings are, respectively, produced through an efficient dual-resolution (DR) and a single-coarse-resolution (SCR) EnVar ingesting a 2-km ensemble. Both experiments launch 1-h forecasts at 500-m grid spacing. Diagnostics of data assimilation (DA) cycling reveal DR produces stronger and broader rear-flank cold pools, more intense downdrafts and updrafts with finer scales, and more hydrometeors at high altitudes through accumulated differences between two DA algorithms. Relative differences in DR, compared to SCR, include the integration from higher-resolution analyses, the update for higher-resolution backgrounds, and the propagation of ensemble perturbations along higher-resolution model trajectory. Predictions for storm morphology and cold pools are more realistic in DR than in SCR. The DR-TLV tracks match better with the observed tornado tracks than SCR-TLV in timing of intensity variation, and in duration. Additional experiments suggest 1) the analyzed kinematic variables strongly influence timing of intensity variation through affecting both low-level rear-flank outflow and midlevel updraft; 2) potential temperature analysis by DR extends the second track's duration consistent with enhanced low-level stretching, delayed broadening large-scale downdraft, and (or) increased near-surface baroclinic vorticity supply; and 3) hydrometeor analyses have little impact on TLV predictions.

1. Introduction

Accurate prediction of the evolution of a tornado still remains a great challenge. Instead of directly predicting tornadoes, many studies have employed ensemble-based data assimilation (DA) methods to initialize the parent storms that spawn tornadoes by assimilating radar and other observations (e.g., Dowell et al. 2004; Jung et al. 2012; Tanamachi et al. 2013; Yussouf et al. 2013; Wang and Wang 2017). These studies often adopt 1–3 km horizontal grid spacings to produce proxy forecasts of tornado existence inferred from mid- and low-level rotations (Sobash et al. 2016). However, other studies (e.g., Trapp 1999; Markowski et al. 2011; Marquis et al. 2012; Thompson et al. 2015) have shown that the strength and existence of mid- and low-level mesocyclones may not agree well with tornado occurrence, which suggests

the need to explicitly predict tornadoes or tornado-like vortices (TLVs). Given most tornado vortices have a maximum spatial scale less than 2 km (Wurman and Alexander 2004; Wurman and Kosiba 2013), a sub-kilometer (i.e., usually ≤ 500 m) grid spacing is vital to resolve the finescale properties of tornadoes or TLVs.

Some studies (Mashiko et al. 2009; Schenkman et al. 2012; Xue et al. 2014; Schenkman et al. 2014; Dawson et al. 2015; Seko et al. 2015; Hanley et al. 2016) have attempted to predict or simulate tornadoes or TLVs with a subkilometer grid spacing. For instance, a tornado in Typhoon Shanshan was simulated in Mashiko et al. (2009) at a 50-m grid spacing. Their simulation was initialized by downscaling initial conditions (ICs) at 5-km grid spacing. Schenkman et al. (2012) simulated a TLV on a 100-m resolution grid nested from 400-m ICs and documented in detail the process of the tornadogenesis. In separate case studies, Xue et al. (2014) and Schenkman et al. (2014) used a 50-m grid, downscaled from a 1-km

Corresponding author: Xuguang Wang, xuguang.wang@ou.edu

analysis, to produce F3-intensity tornadoes. In these studies, the simulated tornadoes had an approximately 8-km displacement in location compared to the observed long-lived F4-intensity tornado. A similar study with 100- and 200-m grid spacings initialized from ICs at 2.2-km grid spacing was conducted to simulate TLVs using the Unified Model from the Met Office (Hanley et al. 2016). Dawson et al. (2015) utilized a simulation at a 250-m grid spacing initialized from a 1-h forecast at 1-km horizontal grid spacing to investigate the sensitivity of TLV to the microphysics schemes. Each of these studies showed that TLVs can be produced with simulations at a subkilometer grid spacing; however, they initialize simulations from coarser-resolution ICs, most at grid spacings greater than 1 km. Downscaling ICs from a coarser resolution may lose the finer-scale characteristics associated with the TLV. Potvin et al. (2017) examined the impact of IC resolution on TLV prediction by using a simulation framework where the truth simulation is known and by generating ICs at various resolutions through filtering the simulated truth. They found the subsequent TLV simulation is relatively insensitive to the resolution of the ICs. The present study is the first to examine the impact of using an IC at a subkilometer versus kilometer grid spacing on the prediction of TLV for the 8 May 2003 Oklahoma City (OKC) tornadic supercell case. In the present study the ICs are produced directly from a cycled DA system. The subkilometer grid spacing DA experiment was realized by extending the dual-resolution GSI ensemble-based variational (EnVar) system.

Ensemble-based DA systems involve running multiple ensemble member forecasts to create flow-dependent background error covariance, which can be computationally expensive especially with increasing model resolution. For example, Marquis et al. (2014) acknowledged the challenge of running all background ensemble members at a subkilometer grid spacing due to the large computational cost. To reduce the cost, several studies have either proposed or implemented a dual-resolution (DR) approach where a high-resolution first guess at a kilometer grid spacing is updated by using a coarser-resolution ensemble in a pure ensemble Kalman filter (Gao and Xue 2008; Rainwater and Hunt 2013) or an EnVar hybrid DA system (Schwartz et al. 2015; Schwartz 2016; Lu et al. 2017; Potvin et al. 2017; Kay and Wang 2020). None of these studies, however, extended the DR approach to generate analyses at a subkilometer grid spacing to study the impact of using the subkilometer grid spacing ICs for TLV prediction. In the present study, we further extend the DR capability of the GSI-based EnVar system for convective-scale DA and predictions at a subkilometer grid spacing. In particular, we adopt the extended system to address the following question: What is the impact of initializing from

an analysis at a subkilometer grid spacing versus an analysis at a kilometer grid spacing on the subsequent prediction of TLVs embedded in the 8 May 2003 OKC tornadic supercell? The DR extension was made in the GSI-based EnVar with the direct radar radial velocity and reflectivity assimilation capability proposed and implemented by Wang and Wang (2017). Two experiments are designed and performed to address the proposed question. In the first experiment, a DR EnVar is implemented which produces the high-resolution ICs at a 500-m grid spacing while ingesting a coarser-resolution ensemble at a 2-km grid spacing to estimate the background error covariance. The second experiment adopts a single-coarse-resolution (SCR) EnVar where the ICs are produced at a 2-km grid spacing ingesting an ensemble at the same 2-km grid spacing. The subsequent simulation in the SCR experiment is run at a 500-m grid spacing initialized from the downscaled 2-km analysis. Such an experimental design allows us to investigate the proposed question from both the DA algorithm differences point of view and from a storm dynamics and thermodynamics point of view. Note that this study does not aim to provide a comprehensive theory on tornadogenesis or evolution. Rather, a hypothesis based on a qualitative diagnostic is aimed at facilitating a physical understanding of the proposed question.

The rest of the paper is organized as follows. Section 2 briefly introduces the 8 May 2003 OKC tornadic supercell and its embedded tornadoes. In section 3, we describe the formulations of the DR method in GSI-based EnVar and the setup of the DA and forecast experiments. Section 4 first describes the differences of the ICs produced by SCR and DR, followed by detailed diagnostics on DA cycling to understand the causes of the differences in the ICs. Furthermore, section 4 discusses additional sensitivity experiments and diagnostics to reveal how the differences in ICs are translated into the subsequent forecast differences in durations, and intensity variations along the TLV tracks. Section 5 summarizes the paper.

2. Case overview

The 8 May 2003 OKC tornadic supercell thunderstorms have been investigated by a series of studies, including Romine et al. (2008), Hu and Xue (2007), Yussouf et al. (2013), Xue et al. (2014), and Wang and Wang (2017). An isolated supercell developed along a dryline located in west-central Oklahoma, identified by a pronounced hook appendage at around 2200 UTC. This supercell storm moved toward the east-northeast and started to decay after 2300 UTC, dissipating over an hour later by 0020 UTC 9 May. According to the official
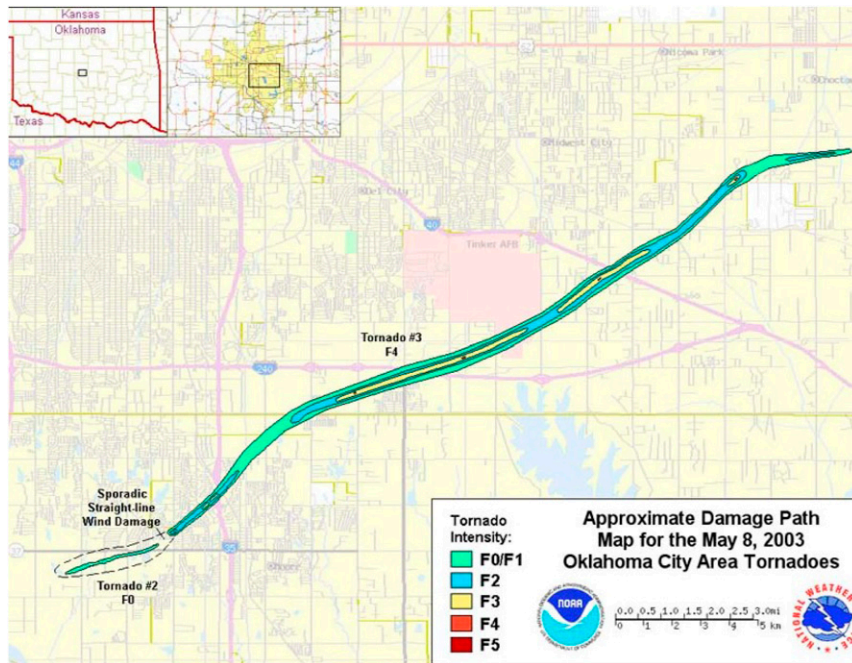
FIG. 1. The observed damage path of the 8 May 2003 Oklahoma City (OKC) tornado overlaid on the map of the Moore–south OKC area. Image is obtained from the National Weather Service website (https://www.weather.gov/oun/events-20030508).

National Weather Service (NWS) survey results,[1] this supercell produced three tornadoes that passed through Moore, southern Oklahoma City, Midwest City, and Choctaw, Oklahoma. The first reported tornado existed for 1 min from 2200 to 2201 UTC with a damage path of about 0.3 km but was not discernable in any WSR-88D radar products (Romine et al. 2008). The segmented paths produced by the second and third tornadoes listed in the National Climatic Data Center Storm Data publication (NCDC 2003, 340–342) are shown in Fig. 1. An F0 tornado formed southwest of Moore and lasted from 2204 to 2208 UTC, tracking on the ground for about 3 km. Within the same storm, a third stronger F2–F4 scale tornado formed at 2210 UTC and dissipated at 2238 UTC with a ~30 km east-northeast track. The third tornado received more attention in previous work (Schenkman et al. 2012; Xue et al. 2014) than the second one, as the second one was weak and short lived. However, different from these studies, the examined tornado predictions in this work include the periods for both the second and third tornadoes. Burgess et al. (2005) and other studies (Burgess 2004; Romine et al. 2008) mentioned that a continued tornado-scale vortex

persisted from 2204 to 2238 UTC according to the observations from the Terminal Doppler Weather Radar at Will Rogers World Airport, Oklahoma City (TDWR), despite two damage tracks were generated. This study will focus on how the intensity variation of simulated surface vorticity is aligned with that along observed damage tracks.

3. Methodology and experiment design

a. GSI-based dual-resolution EnVar algorithm

The DR EnVar system has been introduced and implemented for different EnVar DA systems and experimented with various phenomena, such as the precipitation forecasts in the Weather Research and Forecasting Model data assimilation system (WRFDA) by Schwartz et al. (2015) and the hurricane predictions in GSI by Lu et al. (2017). This study extends the DR capability of the GSI-based EnVar for TLV predictions with the analysis produced at a subkilometer grid spacing. The GSI EnVar DA system has been extended with the capability to directly assimilate both the radial velocity and radar reflectivity observations (Wang and Wang 2017). Pure ensemble covariance is used in this GSI-based DR EnVar and its formulations are briefly described as follows. The notations largely follow Wang (2010) and Schwartz et al. (2015).

---

[1] The NWS report for the 8 May 2003 Oklahoma City tornadic supercell is summarized in https://www.weather.gov/oun/events-20030508.

The EnVar obtains the analysis increment $\mathbf{x}'$ by minimizing the following cost function:

$$J(\mathbf{a}) = 0.5(\mathbf{a})^{\mathrm{T}}\mathbf{A}^{-1}(\mathbf{a}) + 0.5(\mathbf{y}^{o'} - \mathbf{H}\mathbf{x}')^{\mathrm{T}}\mathbf{R}^{-1}(\mathbf{y}^{o'} - \mathbf{H}\mathbf{x}'). \tag{1}$$

On the right-hand side of Eq. (1), the localization for the ensemble covariance is defined in the block-diagonal matrix $\mathbf{A}$; the vector $\mathbf{a}$ is formed by concatenating the nondimensional control vectors $\mathbf{a}_k$, $k = 1, \ldots K$, in which K denotes the ensemble size. The last term of Eq. (1) is the observation term, where $\mathbf{R}$ is the observation error covariance matrix, $\mathbf{H}$ is the linearization of the nonlinear observation operator, and $\mathbf{y}^{o'}$ is the innovation vector measuring the deviation between the observation and its first guess. Here we define the analysis increment $\mathbf{x}'$ as

$$\mathbf{x}' = \mathbf{V}\mathbf{D}\mathbf{a}. \tag{2}$$

The matrix $\mathbf{D}$ is formulated by $[\mathrm{diag}(\mathbf{x}_1^e) \cdots \mathrm{diag}(\mathbf{x}_k^e)]$ and $\mathbf{x}_k^e$ denotes the kth ensemble perturbation normalized by $\sqrt{K-1}$. The operator $\mathbf{V}$ is adopted to interpolate vector $\mathbf{D}\mathbf{a}$ from at a coarse resolution to at a fine resolution.

In the aforementioned equations, $\mathbf{x}_k^e$ and $\mathbf{a}_k$ are vectors of length n_e, and vector $\mathbf{x}'$ has a length n_c. Length n_e represents the number of state variables used in the ensemble perturbation, while length n_c is the number of state variables associated with the analysis increment. $\mathbf{D}$ is a $n_e \times Kn_e$ matrix, $\mathbf{a}$ is a vector of length Kn_e, and the vector $\mathbf{D}\mathbf{a}$ has a length n_e. In SCR EnVar system, where the ensemble member and control are at the same resolution, $\mathbf{V}$ is an identity matrix with the size of $n_e = n_c$. In the DR EnVar system, usually $n_c > n_e$. The interpolation operator $\mathbf{V}$ in this case has a dimension of $n_c \times n_e$. Following Wang (2010), the gradient of Eq. (1) with respect to the extended control variable $\mathbf{a}$ can be derived as

$$\nabla_a J = \mathbf{A}^{-1}\mathbf{a} + \mathbf{D}^{\mathrm{T}}\mathbf{V}^{\mathrm{T}}\mathbf{H}^{\mathrm{T}}\mathbf{R}^{-1}(\mathbf{H}\mathbf{x}' - \mathbf{y}^{o'}). \tag{3}$$

In Eq. (3) $\mathbf{V}^{\mathrm{T}}$, the adjoint matrix of $\mathbf{V}$ with a dimension of $n_e \times n_c$, is applied to convert $\mathbf{H}^{\mathrm{T}}\mathbf{R}^{-1}(\mathbf{H}\mathbf{x}' - \mathbf{y}^{o'})$ from a fine grid to a coarse grid. During the variational minimization, $\mathbf{V}^{\mathrm{T}}$ and $\mathbf{V}$ are applied to $\mathbf{H}^{\mathrm{T}}\mathbf{R}^{-1}(\mathbf{H}\mathbf{x}' - \mathbf{y}^{o'})$ and $\mathbf{D}\mathbf{a}$ for each iteration, respectively. It is noted that the above formulations are also valid for the SCR EnVar if $\mathbf{V}^{\mathrm{T}}$ and $\mathbf{V}$ are identity matrices. Therefore, Eqs. (2) and (3) are the general expressions for both SCR and DR EnVar.

After the DA procedures, a control analysis at a subkilometer grid spacing is produced by DR EnVar, while the control analysis in SCR EnVar uses a kilometer grid spacing. Thus the finer-scale processes and features are better resolved with DR EnVar than SCR
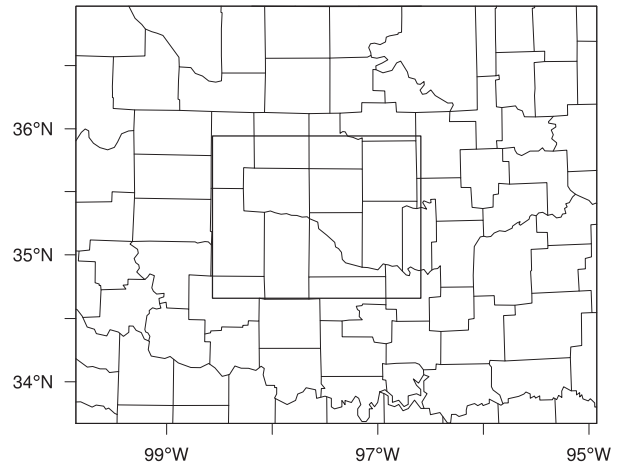

FIG. 2. The 2-km/500-m nested domain for data assimilation and free forecast.

EnVar during the DA cycling. In our experiment design, the same observations are assimilated in both configurations. Given that the radial resolution of the WSR-88D radar observation can reach 250 m, a subkilometer grid spacing analysis can better ingest the information from such observations than a kilometer grid spacing analysis.

b. Configuration of data assimilation and forecast experiments

Version 3.6.1 of WRF-ARW is adopted with a two-way nested domain for experiments in this study (Fig. 2). The outer domain has 226×181 horizontal grid points with a 2-km grid spacing, and the inner domain has 361×281 horizontal grid points with a 500-m grid spacing. The number of vertical levels is set to 50. The same physics schemes are used for both domains. Specifically, the model employs the Thompson microphysics scheme (Thompson et al. 2008), the Mellor–Yamada–Janjić planetary boundary layer scheme (Mellor and Yamada 1982; Janjić 1990, 1994, 2002), the Noah land surface model (Chen and Dudhia 2001), and the Rapid Radiative Transfer Model for general circulation models schemes (RRTMG; Iacono et al. 2008) as the longwave and shortwave radiation schemes.

Both radar reflectivity and radial velocity are assimilated in this study. These radar observations were retrieved from the National Climatic Data Center (NCDC) archive. The Warning Decision Support System-Integrated Information (WDSSII; Lakshmanan et al. 2007) utility is adopted for the quality control of these radar data. Spurious reflectivity in the model is intended to be suppressed by assimilating the "non-precipitation" radar observations and setting all
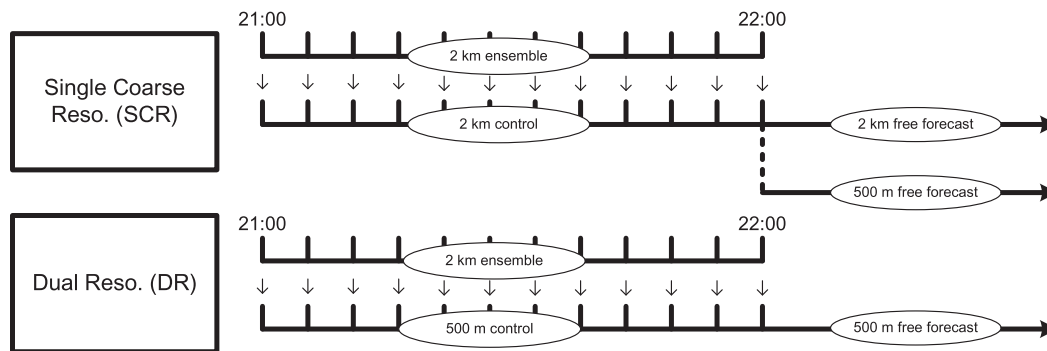
FIG. 3. Schematics of the analyses and forecasts for Exp-SCR and Exp-DR. Both experiments assimilate the radar data every 5 min from 2100 to 2200 UTC. The analyses at 2-km and 500-m grid spacings are, respectively, generated in Exp-SCR and Exp-DR by ingesting an ensemble at a 2-km grid spacing. To be comparable with DR, the analysis from SCR is downscaled to 500-m grid. Two 1-h 500-m forecasts are then initialized by both analyses at 2200 UTC after 1-h assimilation.

observed reflectivity lower than 5 to 0 dBZ prior to assimilation. The observation errors for radar reflectivity and radial velocity are defined as 5 dBZ and 2 m s^{-1}, respectively.

By assimilating radar radial velocity and reflectivity, the two-way coupled GSI-based SCR and DR EnVar systems are applied to directly produce ICs at a 2-km grid spacing (Exp-SCR) and at a 500-m grid spacing (Exp-DR), respectively. Such a two-way coupled GSI-based EnVar DA system has been applied for the operational Global Forecast System [e.g., Fig. 1b of Wang et al. (2013)] and for the operational Hurricane Weather Research and Forecasting (HWRF) model [Fig. 1 of Lu et al. (2017)]. Both experiments are conducted with similar procedures except the grid spacing of the control analysis and background forecast where a grid spacing of 500 m is used for the Exp-DR and a grid spacing of 2 km for Exp-SCR. Both systems ingest a 45-member ensemble at a 2-km grid spacing. The flowcharts of the radar DA and the subsequent forecasts for the two experiments are shown in Fig. 3. Similar to Wang and Wang (2017), the radar observations are assimilated every 5 min from 2100 to 2200 UTC 8 May 2003. For Exp-SCR, the 2-km control analysis generated from the final DA cycle valid at 2200 UTC is downscaled to a 500-m grid before initializing a free forecast. Such downscaling of a coarser-resolution analysis is the general application in previous TLV prediction studies (Mashiko et al. 2009; Schenkman et al. 2012; Xue et al. 2014; Schenkman et al. 2014; Dawson et al. 2015; Hanley et al. 2016). Together with the 500-m control analysis directly produced from Exp-DR, two 1-h high-resolution TLV deterministic forecasts are launched at a 500-m grid spacing for both Exp-SCR and Exp-DR.

During the DA cycling, following the flowchart of a two way coupled hybrid DA system [Fig. 1b of

Wang et al. (2013)], the control first guess is updated using EnVar (Wang 2010; Wang and Wang 2017) by ingesting ensemble perturbations to estimate the background error covariance, while the ensemble first guess perturbations are updated by the ensemble square root filter (EnSRF; Whitaker and Hamill 2002). The final ensemble analyses are obtained by recentering the EnSRF ensemble analyses around the control analysis following Wang et al. (2013). Specifically in Exp-DR, the 2-km control analysis is replaced by the 500-m control analysis through a two-way nest run, and then is used to recenter the 2-km EnSRF ensemble analyses. The same DA parameters are applied for both Exp-SCR and Exp-DR. The localization scales are 12 km in the horizontal and 1.1 scale height in the vertical. As in Wang and Wang (2017), equivalent cutoff distances are used in EnVar and EnSRF. The analysis perturbations are inflated so that the final posterior ensemble spread is 90% of the prior ensemble spread (Whitaker and Hamill 2012). In addition to increasing the spread of the first guess ensemble, smoothed constant inflation and additive noise (Whitaker et al. 2008; Dowell and Wicker 2009; Dowell et al. 2011; Dawson et al. 2012; Jung et al. 2012; Wang et al. 2013; Yussouf et al. 2013; Wang and Wang 2017) with both horizontal and vertical length scales of 3 km are applied in regions where the observed radar reflectivity exceeds 25 dBZ. Constant inflation with a coefficient of 1.04 is applied to each ensemble perturbation in each DA cycle. Additive noise with standard deviations of 0.5 m s^{-1}, 0.5 K, and 0.5 K (Yussouf et al. 2013; Wang and Wang 2017) are, respectively, added to the horizontal winds, temperature, and dewpoint fields for the first six DA cycles. After applying the constant inflation and additive noise techniques, the analyses are further advanced
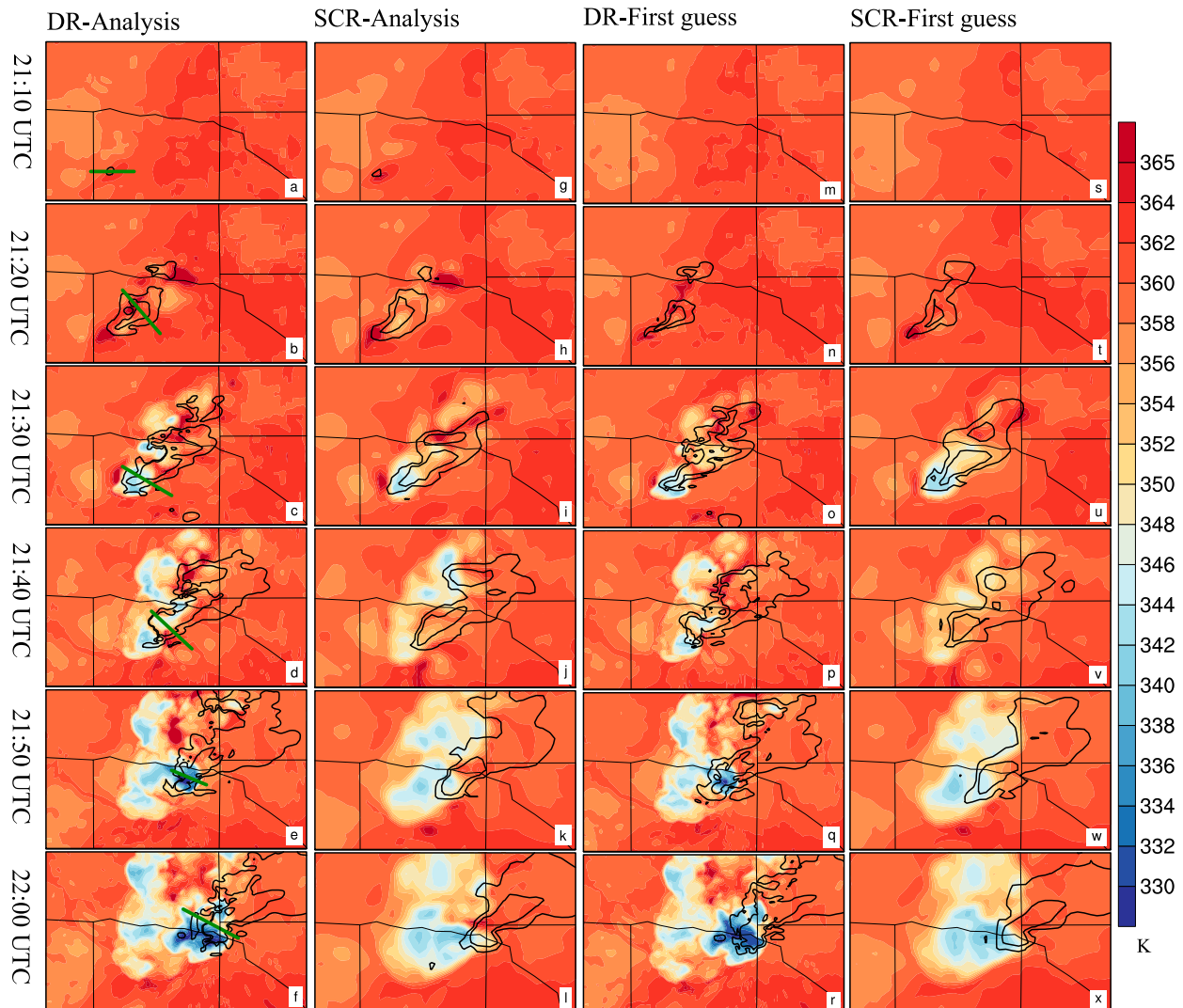
FIG. 4. The reflectivity (contours from 20 to 60 dBZ at 20 dBZ intervals; dBZ) at 1 km AGL and surface equivalent potential temperature (colors; K) (a)–(l) analysis and (m)–(x) first guess for (a)–(f),(m)–(r) Exp-DR and (g)–(l),(s)–(x) Exp-SCR from data assimilation cycles valid at 2110, 2120, 2130, 2140, 2150, and 2200 UTC, respectively. Green lines in the first column represent the positions of 0–12 km AGL vertical cross sections in Fig. 5. These greens lines are selected across the maximum reflectivity at 1 km AGL.

for 5 min to establish the flow-dependent structure (Wang et al. 2013; Wang and Wang 2017).

4. Results

a. Comparison of DR and SCR EnVar during the DA cycling

To understand the impacts of DR versus SCR EnVar on the final control analysis, both the first guess and analysis from Exp-DR are compared with those from Exp-SCR during the DA cycling in Figs. 4 and 5. After 6 DA cycles, the two experiments both spin up the storm and reach a similar horizontal coverage of reflectivity at about 2130 UTC (Figs. 4c,i,o,u). During the early spinup

period, both experiments generate similar cold pools and reflectivity fields at low levels (Figs. 4a,b vs Figs. 4g,h), as well as similar upper-level vertical motions (Figs. 5a,b vs Figs. 5g,h). Starting from 2130 UTC, the vertical motion and reflectivity at upper levels (Figs. 5d–f vs Figs. 5j–l) and the cold pool over the rear-flank (RF) region (Figs. 4d–f vs Figs. 4j–l) become remarkably different between the two experiments. For example, Exp-DR produces an updraft in the upper levels (i.e., 7 km AGL) that is more than $10 \, \text{m s}^{-1}$ stronger than Exp-SCR (Fig. 5f vs Fig. 5l). It also produces a downdraft below 3 km AGL that is $\sim 4 \, \text{m s}^{-1}$ stronger than Exp-SCR (Fig. 5e vs Fig. 5k). Accompanying the stronger updraft, more hydrometeors are elevated to
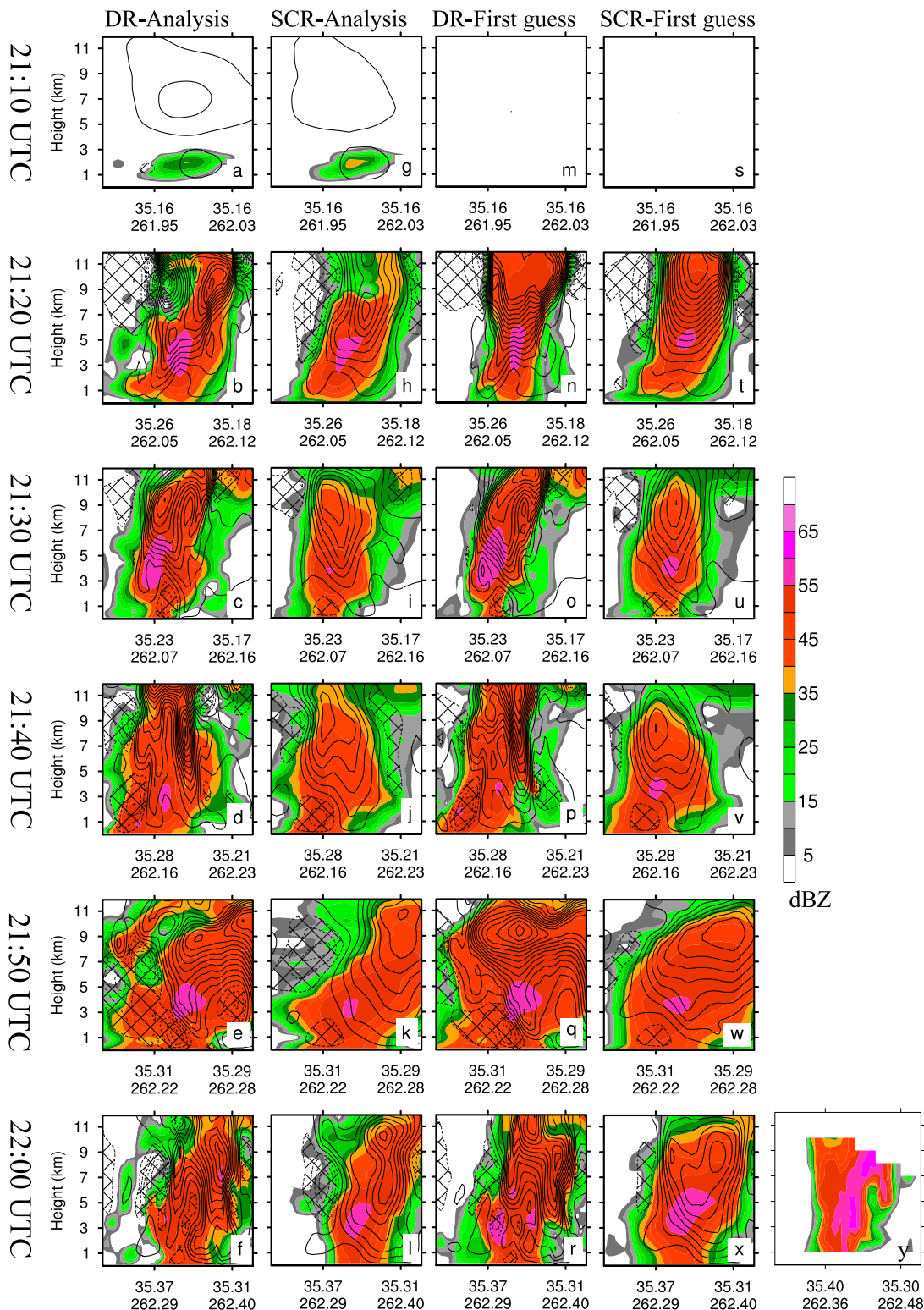
FIG. 5. Vertical cross sections of reflectivity (colors; dBZ) and vertical motions (contours from −38 to 50 m s^{-1} at 4 intervals; m s^{-1}) (a)–(l) analysis and (m)–(x) first guess for (a)–(f),(m)–(r) Exp-DR and (g)–(l),(s)–(x) Exp-SCR from data assimilation cycles valid at 2110, 2120, 2130, 2140, 2150, and 2200 UTC 8 May 2003, respectively. (y) Vertical section of observed reflectivity (colors; dBZ) valid at 2200 UTC across its surface maxima. Solid contours (pattern shading) represent upward (downward) velocity.
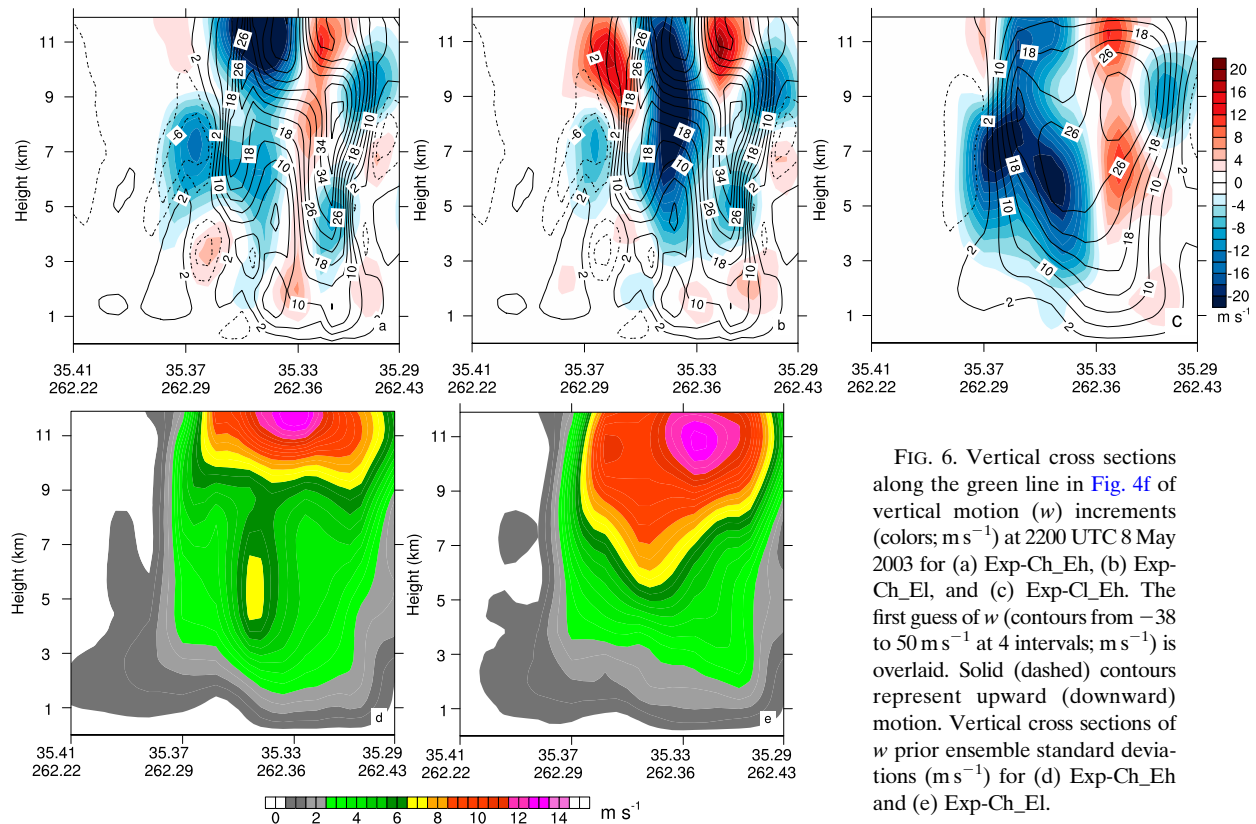
FIG. 6. Vertical cross sections along the green line in Fig. 4f of vertical motion (w) increments (colors; m s^{-1}) at 2200 UTC 8 May 2003 for (a) Exp-Ch_Eh, (b) Exp-Ch_El, and (c) Exp-Cl_Eh. The first guess of w (contours from −38 to 50 m s^{-1} at 4 intervals; m s^{-1}) is overlaid. Solid (dashed) contours represent upward (downward) motion. Vertical cross sections of w prior ensemble standard deviations (m s^{-1}) for (d) Exp-Ch_Eh and (e) Exp-Ch_El.

higher altitudes in Exp-DR, which produces ∼10 dBZ higher reflectivity above 7 km AGL (Fig. 5f vs Fig. 5l). The RF cold pool in Exp-DR is ∼10 K colder than in Exp-SCR (Fig. 4e vs Fig. 4k). In general, the cold pool temperature can be greatly reduced through enhanced precipitation loading and the associated increased cooling by evaporation and melting (Dowell et al. 2011; Yussouf et al. 2013). The greater enhancement for the cold pool in Exp-DR relative to Exp-SCR corresponds well with the stronger downdrafts below 3 km AGL (Figs. 5d–f,p–r vs Figs. 6j–l,v–x). These differences become increasingly pronounced after 2140 UTC, suggesting that the differences at the final analysis are an accumulated effect from the preceding DA cycles.

We speculate that the final analysis difference is caused by the following differences in the DR and SCR DA algorithms. Both systems use the ensemble background at the same 2-km grid spacing. As the control background forecast in Exp-DR uses a higher resolution, its first guess is expected to better depict finer-scale features associated with the supercell development (e.g., Adlerman and Droegemeier 2002; Noda and Niino 2003; Fiori et al. 2010) and to better compare against the high-resolution observations for the innovation calculation relative to Exp-SCR. Moreover, the recentering procedure

adopted in our two-way coupled EnVar DA system implicitly allows the coarse-resolution background ensemble to propagate along the high-resolution control trajectory. Mathematically, the terms related to the ensemble covariance and the innovation vector, expressed as **D** and $\mathbf{y}^{o'}$ in Eq. (1) are different between the two algorithms.

To reveal the impact of the differences in ensemble covariances and observation innovations between Exp-DR and Exp-SCR on their own analyses, three one cycle DA experiments with the analysis valid at 2200 UTC 8 May 2003 are designed (Table 1). In Exp-Ch_Eh, the configuration of the control first guess (FG) and the ensemble background is the same as Exp-DR. Exp-Ch_El is the same as Exp-DR except that the preceding analysis ensemble valid at 2155 UTC is recentered around a 2-km control analysis rather than a 500-m control analysis. Therefore, during the subsequent 5-min first guess forecasts, the ensemble first guess in Exp-Ch_Eh evolves implicitly along with the trajectory of a 500-m grid whereas Exp-Ch_El implicitly evolves with the trajectory of a 2-km grid. Due to nonlinearity, the ensemble perturbations valid at 2200 UTC are therefore different. Compared to Exp-Ch_El (Fig. 6e), the Exp-Ch_Eh (Fig. 6d) spread of vertical velocity (w) is broadly smaller above 3 km AGL and has more finescale details between 3 and 7 km AGL.

TABLE 1. List of EnVar tests and their configurations for control first guess (FG) and ensemble. The analysis time is valid at 2200 UTC 8 May 2003. The 500-m and 2-km control FGs are generated through advancing the 500-m and 2-km control analyses valid at 2155 UTC from Exp-DR with two-way nesting for 5 min. Both ensembles used in Exp-Ch_Eh and Exp-Ch_El are initialized from the ensemble analysis valid at 2155 UTC, despite which are recentered around the 500-m and 2-km control analyses, respectively.

| | Input configuration | |
Expt	Control FG	Ensemble
Exp-Ch_Eh[a]	500-m control FG	2-km ensemble evolving along the trajectory of a 500-m control grid
Exp-Ch_El	Same as Exp-Ch_Eh	2-km ensemble evolving along the trajectory of a 2-km control grid
Exp-Cl_Eh	2-km control FG	Same as Exp-Ch_Eh

[a] Exp-Ch_Eh, a single cycle experiment, uses the same configuration of control first guess and ensemble background as Exp-DR.

Under 3 km AGL, the spread is larger in Exp-Ch_Eh. Consistently, the Exp-Ch_Eh w increments are smaller above 3 km AGL than in Exp-Ch_El. In contrast, Exp-Ch_Eh has w increments below 3 km AGL that are 2–4 m s^{-1} greater than in Exp-Ch_El. Therefore, Exp-Ch_Eh has more enhanced downdraft and updraft couplets at low levels over the rear-flank area. As shown later in section 4c and in previous tornado simulation studies (e.g., Marquis et al. 2016), the low-level updraft-downdraft couplet's structure commonly persists around tornadoes.

The impact of the innovation differences is examined in the third experiment, Exp-Cl_Eh. Exp-Cl_Eh only differs from Exp-Ch_Eh by the control first guess valid at 2200 UTC. During 2155–2200 UTC, the 500-m and 2-km control FGs are produced simultaneously with a two-way nesting. Therefore, the simulated storm features are the same in both FGs except that the 2-km grid spacing produces a more smoothed field. The difference of w increments between Exp-Ch_Eh and Exp-Cl_Eh is shown in Fig. 6. Exp-Cl_Eh has more smoothed w increments than Exp-Ch_Eh throughout all vertical levels. The low-level updraft-downdraft couplet's structure in the w increments is much less pronounced in Exp-Cl_Eh. These experiments suggest that the algorithm differences between Exp-DR and Exp-SCR can accumulate during the DA cycling which contributes to the notable final analysis differences.

The differences of the final analysis between Exp-DR and Exp-SCR at 2200 UTC 8 May 2003 are shown in Figs. 5f, 5l, and 7. Specifically, Exp-SCR generally has the more smoothed updraft and downdraft distributions than Exp-DR at 2 km AGL (Figs. 7a,b). The maximum downdraft in Exp-DR is ~6 m s^{-1} greater than in Exp-SCR; the Exp-DR coverage of the strong updraft is more widespread than Exp-SCR. Consistent with the greater upper-level updraft in Exp-DR, more reflectivity is found at high altitudes in Exp-DR (Figs. 5f,l). The Exp-DR reflectivity above 7 km AGL is ~10 dBZ larger than Exp-SCR. Larger reflectivity at high altitudes in Exp-DR is more consistent with observations (Fig. 5y), indicating that the stronger upper-level updraft in Exp-DR may be

more consistent with reality. Near the ground, a more widespread RF cold pool with colder air is produced in Exp-DR relative to Exp-SCR (Figs. 7c,d). The minimum equivalent potential temperature over the RF area of Exp-DR is more than 20 K lower than that of Exp-SCR. Rather limited surface observations are available in the cold pool area at the analysis time. In both experiments, the Oklahoma City (KOKC) METAR station observation is found in the east edge of the cold pool (Fig. 11) near the analysis time. The analyzed equivalent potential temperature (θ_e) at KOKC in Exp-DR is ~2 K colder than in Exp-SCR and closer to the observation, despite the fact that it is still ~7 K warmer than the reality at 2159 UTC (Fig. 8a). This KOKC observation demonstrates that the stronger cold pool in Exp-DR is more realistic. Note that we use θ_e in this study to visualize and quantify the cold pools as in Dawson et al. (2010, 2015). It is found there is no significant difference between using θ_e and potential temperature to define the cold pool (not shown).

b. Verification of the predicted storm morphology and cold pool

In this section, two 1-h free forecasts are launched to explore the impacts of the differences in the analysis on the predicted storm morphology. For comparison purpose, the observed reflectivity and radial velocity at the 1.45° elevation of the KTLX radar valid from 2200 to 2230 UTC are plotted at a 10-min interval in Figs. 9a–e and 10a–e, respectively. The corresponding simulated fields from Exp-DR and Exp-SCR in Figs. 9f–o and Figs. 10f–o are mapped onto the same points as observations. Due to the effects of ground clutter in the lowest 0.5° elevation, the 1.45° elevation is applied here to present the low-level storm features.

At the analysis time (2200 UTC), both experiments have a similar storm morphology. Exp-DR produces a slightly better analysis of the areal extent of reflectivity than Exp-SCR (Figs. 9a,f,k). Throughout the period from 2200 to 2230 UTC, this observed supercell storm moves east-northeastward. The predicted storms from
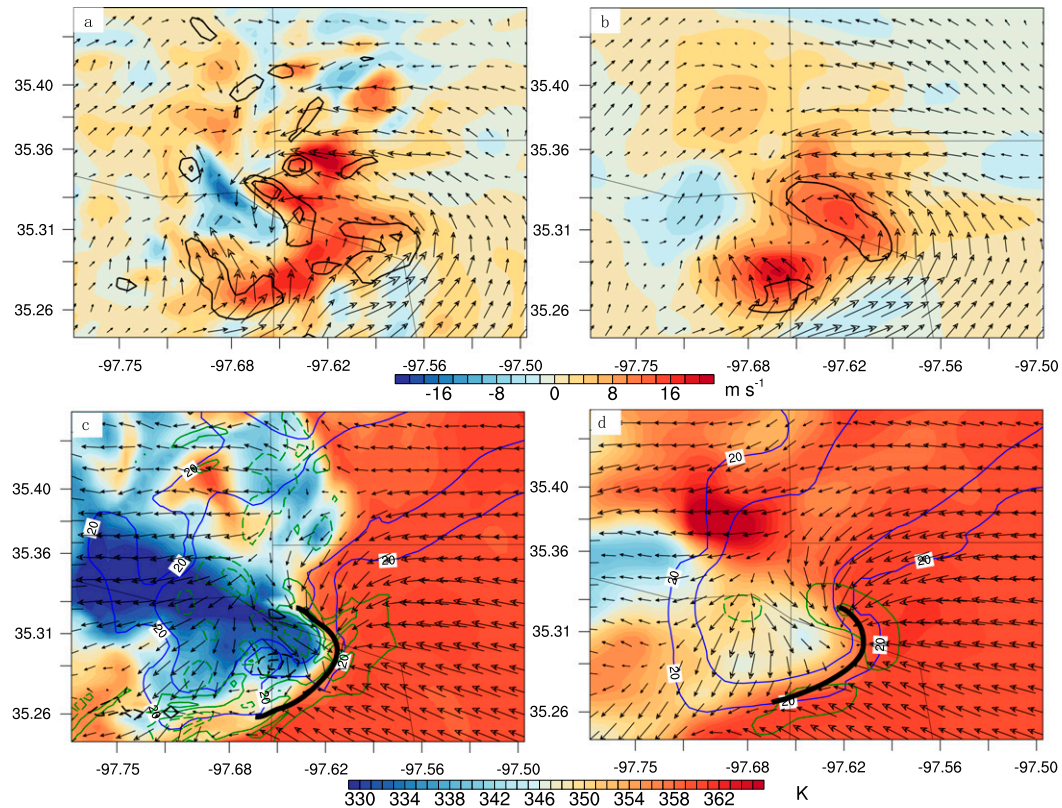
FIG. 7. The vertical velocity (colors; m s^{-1}) and cyclonic vorticity (contours from 0.01 to 0.04 s^{-1} at 0.01 s^{-1} intervals; s^{-1}) at 2 km AGL at the analysis time for (a) Exp-DR and (b) Exp-SCR. The equivalent potential temperature (colors; K), vertical motions (green contours from -3 to 3 m s^{-1} at 1 m s^{-1} interval; m s^{-1}), and reflectivity (blue contours at 20 and 40 dBZ) near the ground valid at 2200 UTC for (c) Exp-DR and (d) Exp-SCR. The position of rear-flank gust front (RFGF; thick black line) are subjectively determined based on the convergence and wind speed fields.

both experiments move in the same direction and at a generally similar speed. The observed hook echo persists more than 30 min from 2200 UTC. The predicted storm in Exp-DR maintains a similar hook echo at the southwest end of the reflectivity core in the same period (Figs. 9f–j); the hook echo in Exp-SCR is only well-defined until 2210 UTC (Figs. 9k–m). Thereafter it becomes less pronounced (Figs. 9n,o). Consistent with the reflectivity, the observed radial velocity differences across the couplet continuously persist from 2200 to 2220 UTC (Figs. 10a–d). The radial velocity couplet is not discernable at 2230 UTC (Fig. 10e) due to its short distance from the radar site. The Exp-DR radial velocity couplet resembles the observations with strong couplets persisting during 2200–2220 UTC. In contrast, the Exp-SCR radial velocity couplet is consistently weaker than Exp-DR and further weakens at 2220 UTC (Fig. 10n). Although both experiments generally have weaker radial velocity couplets than the reality, the couplets in Exp-DR are closer to the observations than in Exp-SCR (Figs. 10f–o). The weaker radial velocity couplets in both experiments may be

attributed to the 500-m grid spacing, which is still insufficient to fully resolve the tornado-scale vortex (Xue et al. 2014).

The predicted cold pools for both experiments from 2201 to 2235 UTC are shown in Fig. 11. The RF cold pool in Exp-DR is consistently stronger ($\sim$6 K colder θ_e) than that in Exp-SCR in the first 20 min lead times (Figs. 11a–e vs Figs. 11i–m). Beginning at 2225 UTC, the rear-flank (RF) cold pool becomes much weaker than before and the forward-flank (FF) cold pool strengths in both experiments. At the KOKC station (Fig. 8a), θ_e in reality sharply decreases from 351 to 336 K during 2159–2211 UTC, which indicates that the cold pool rapidly extended while going through this station. After that, the cold pool near this station is weakened as θ_e gradually gets warmer. Both experiments experience the same processes. However, Exp-DR has a generally 5 K colder cold pool at this station until 2247 UTC and its θ_e is closer to the observations (Fig. 8a) than Exp-SCR. As indicated in Fig. 8b, the observed cold pool starts to pass by the Tinker Air Force Base, Oklahoma (KTIK),
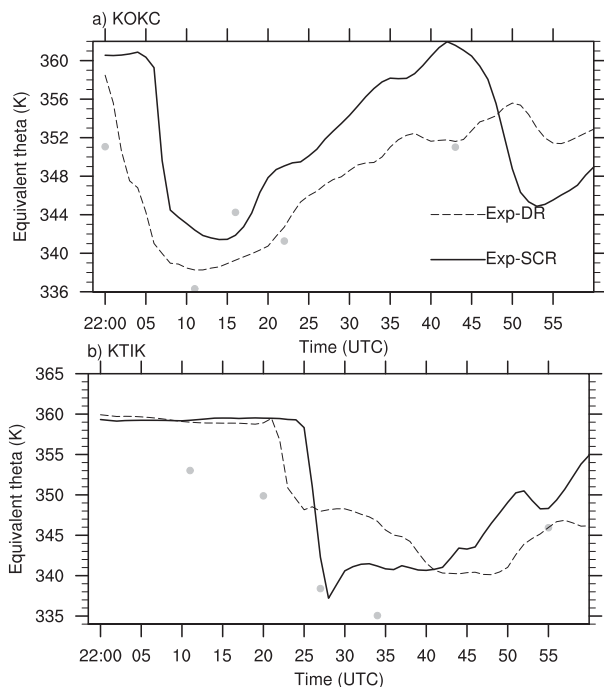
FIG. 8. Equivalent potential temperature (K) from observations (gray dots) and simulations of Exp-DR (dashed) and Exp-SCR (solid) at (a) KOKC and (b) KTIK METAR stations for the period 2200–2300 UTC 8 May 2003. Locations of KOKC and KTIK are marked in Figs. 9 and 11.

station at ~2220 UTC and continues being enhanced at least until 2235 UTC. This trend is better captured by Exp-DR than Exp-SCR, despite Exp-DR still having a warmer cold pool than reality (Fig. 8b). Although the cold pool from Exp-SCR produces a colder temperature that is closer to the observation at 2227 UTC, the temperature trend before and after this time deviates from that of the reality more than Exp-DR.

c. Comparison of the predicted tornado-like vortices (TLVs)

1) COMPARISON OF THE SIMULATED NEAR-SURFACE TLVS

Given that the low-level rotation is used to describe the evolution of tornadoes at low levels in past studies (e.g., Markowski et al. 2012; Marquis et al. 2012, 2016), the simulated near-surface[2] TLV tracks and the time series of the maximum vertical vorticity at the first model level (around 10 m AGL) are examined (Fig. 12). In this study, we have subjectively defined a TLV path with its vorticity at the lowest model level (~10 m AGL)

---

[2] In this study, near-surface or near ground level refers to the first model level at around 10 m AGL.

exceeding $0.03\,\mathrm{s}^{-1}$ in this study. As shown in Figs. 12a and 12b, the TLV paths are determined by the locations of the surface vertical vorticity maxima in the first 40-min forecast period. Exp-DR produces two consecutive TLV tracks with the vertical vorticity greater than $0.03\,\mathrm{s}^{-1}$. It is found that the two simulated tracks are generated along with the weakening and reintensification of the same vortex. The first simulated track is around 2205–2210 UTC and the second is 2213–2232 UTC. These simulated tracks are basically consistent with the observed tornado damage paths, respectively, lasting during 2204–2208 UTC and 2210–2238 UTC, as shown in Fig. 1. The predicted second vorticity path in Exp-DR gradually deviates from the observed track toward the southeast after 2230 UTC. In comparison, Exp-SCR only produces one TLV path with the vertical vorticity greater than $0.03\,\mathrm{s}^{-1}$ during 2205–2218 UTC. The TLV path in Exp-SCR coincides with the observed first tornado damage path in location but persists unrealistically longer than the observation in duration. In addition, the predicted vorticity path increasingly deviates from the observed path and moves southeastward after 2220 UTC.

Note that the purpose of this study is not to explicitly predict the tornadoes as a 500-m horizontal grid spacing is still too low to resolve the tornado-scale vortex (Xue et al. 2014). Instead, trends of changes in the simulated TLV intensity are investigated. Categories on the original Fujita scale are used to measure the strength of the TLV that each simulation can reach. Relative to the single peak of wind speed maxima in Exp-SCR, Exp-DR has two 10-m wind speed peaks, one short lived and one long lived, which better fits the observations. Both experiments produce 10-m wind maxima that reaches or surpasses F1 intensity. In particular, Exp-DR predicts maximum wind, respectively, surpassing and approaching the F1 level during both peak periods, 2205–2209 and 2215–2228 UTC. In contrast, the maximum wind speed in Exp-SCR that reaches the F1 level only persists for a short period from 2205 to 2210 UTC. As shown in Figs. 12c and 12d, the variations of maximum 10-m wind speed resonate with the variation of the vertical vorticity maxima in both experiments. These results reveal that Exp-DR performs better than Exp-SCR in the timing of the intensity variation and in the duration of the TLV.

2) RELATIONSHIPS BETWEEN LOW-LEVEL CONVERGENCE AND NEAR-SURFACE TLV EVOLUTION

To determine the factors that dominate the variation of the near-surface vertical vorticity, the stretching, advection and tilting terms in the vertical vorticity equation are individually examined. The maxima of each quantity within a 1-km horizontal distance of the maximum vertical
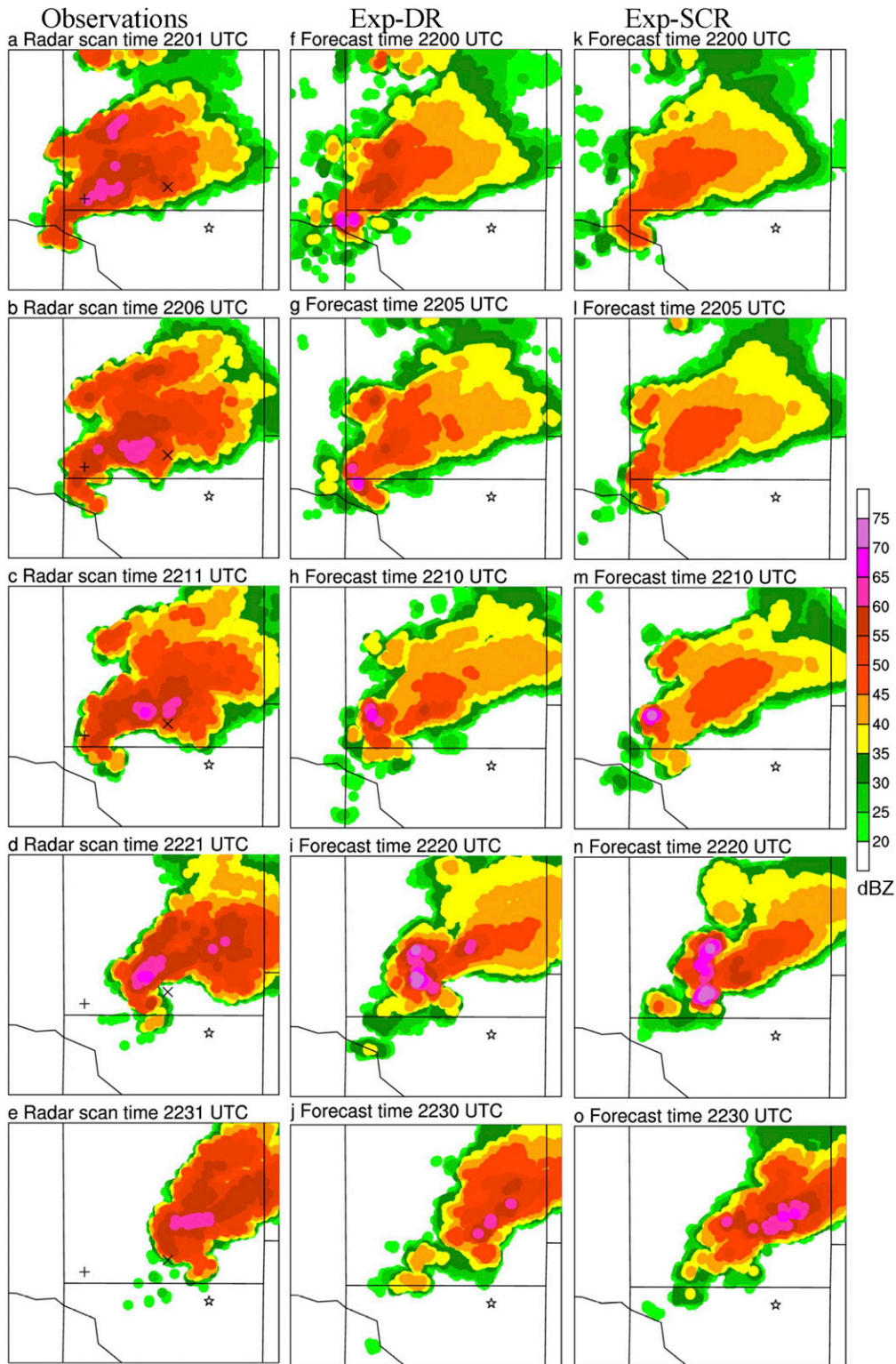
FIG. 9. Reflectivity fields at 1.45° elevation of the KTLX radar for (a)–(e) observations, and experiments (f)–(j) Exp-DR and (k)–(o) Exp-SCR from 2200 to 2230 UTC 8 May 2003. Corresponding times are indicated at the top of each figure. The radar site at Twin Lakes, OK (KTLX), is marked by a star sign. Locations for aviation METAR stations at KOKC and KTIK are labeled with plus and cross signs, respectively.
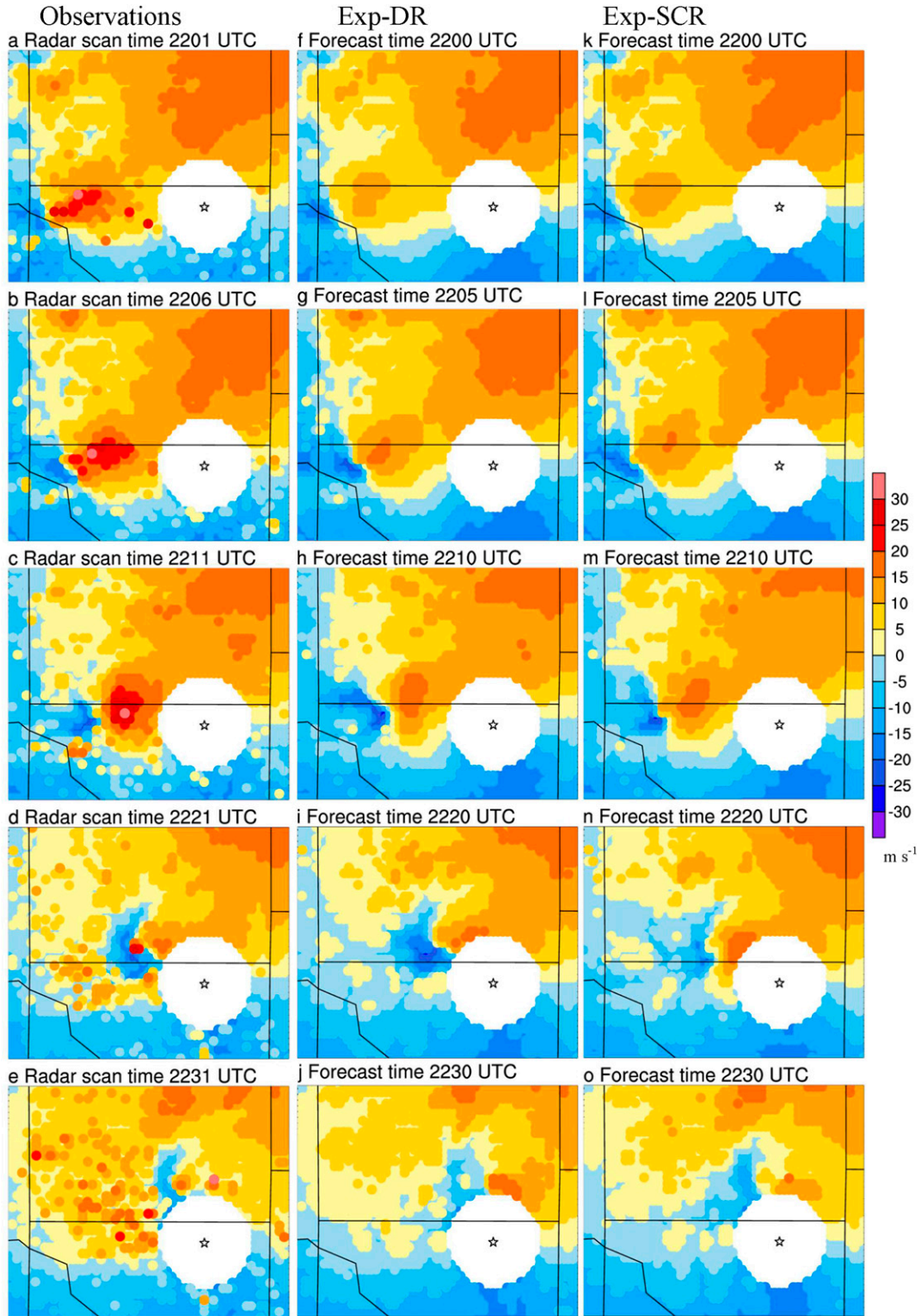
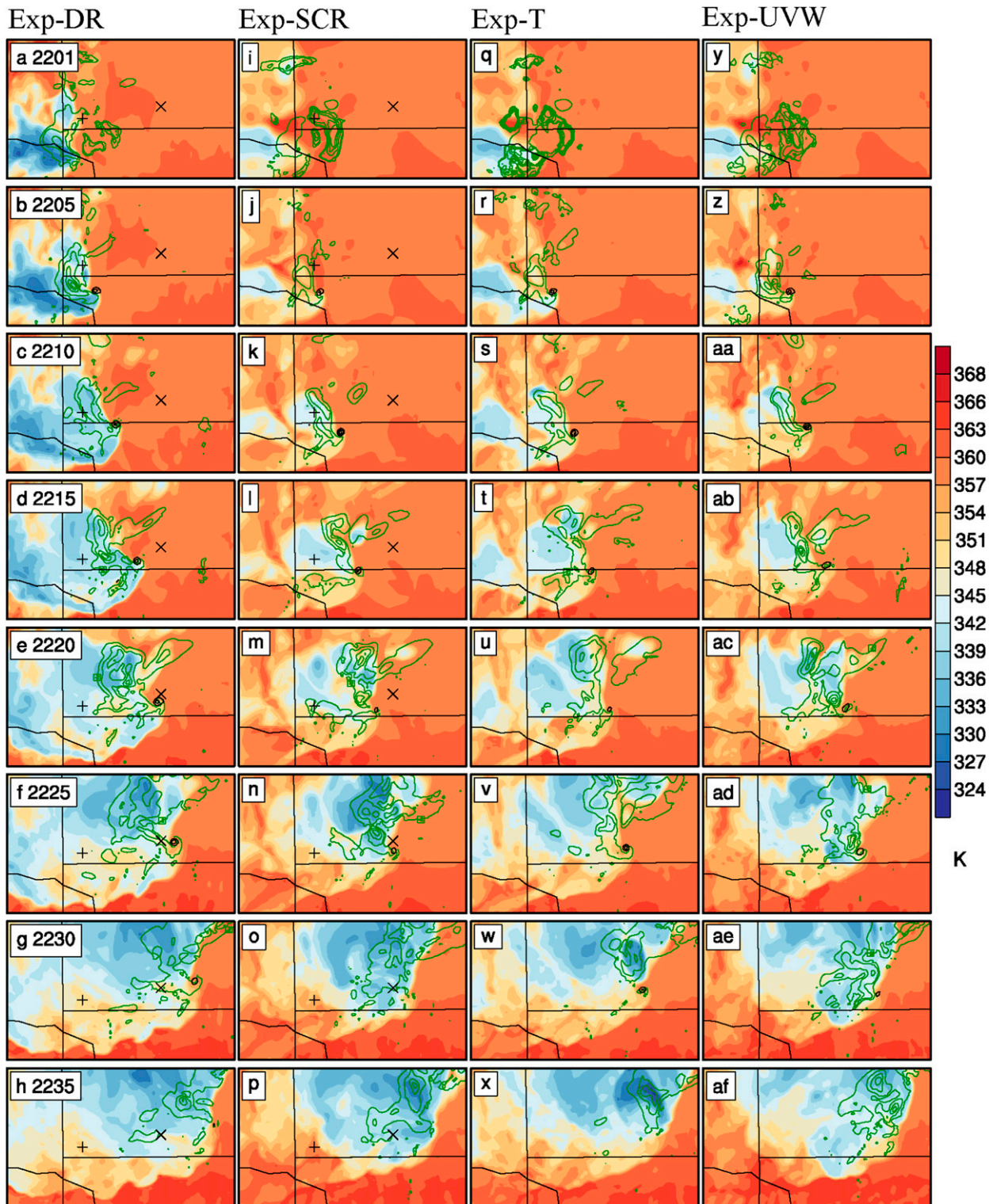FIG. 10. As in Fig. 9, but for the radial velocity (m s^{-1}) fields.

Exp-DR   Exp-SCR   Exp-T   Exp-UVW

FIG. 11. Equivalent potential temperature (colors; K) at the lowest model level (~10 m AGL), vertical vorticity (black contours from 0.02 to 0.08 s^{-1} at 0.02 s^{-1} interval; s^{-1}) at 100 m AGL, and averaged latent cooling rate (green contours from −2 to −30 K min^{-1} at 8 K min^{-1} interval; K min^{-1}) below 1 km AGL for (a)–(h) Exp-DR, (i)–(p) Exp-SCR, (q)–(x) Exp-T, and (y)–(af) Exp-UVW from 2201 to 2235 UTC 8 May 2003. Corresponding forecast time is indicated in each figure of the first column. Locations for aviation METAR stations at KOKC and KTIK are labeled with plus and cross signs, respectively. As the latent cooling rate is calculated during model integration, we use 1-min forecast rather than the analysis in the first row.
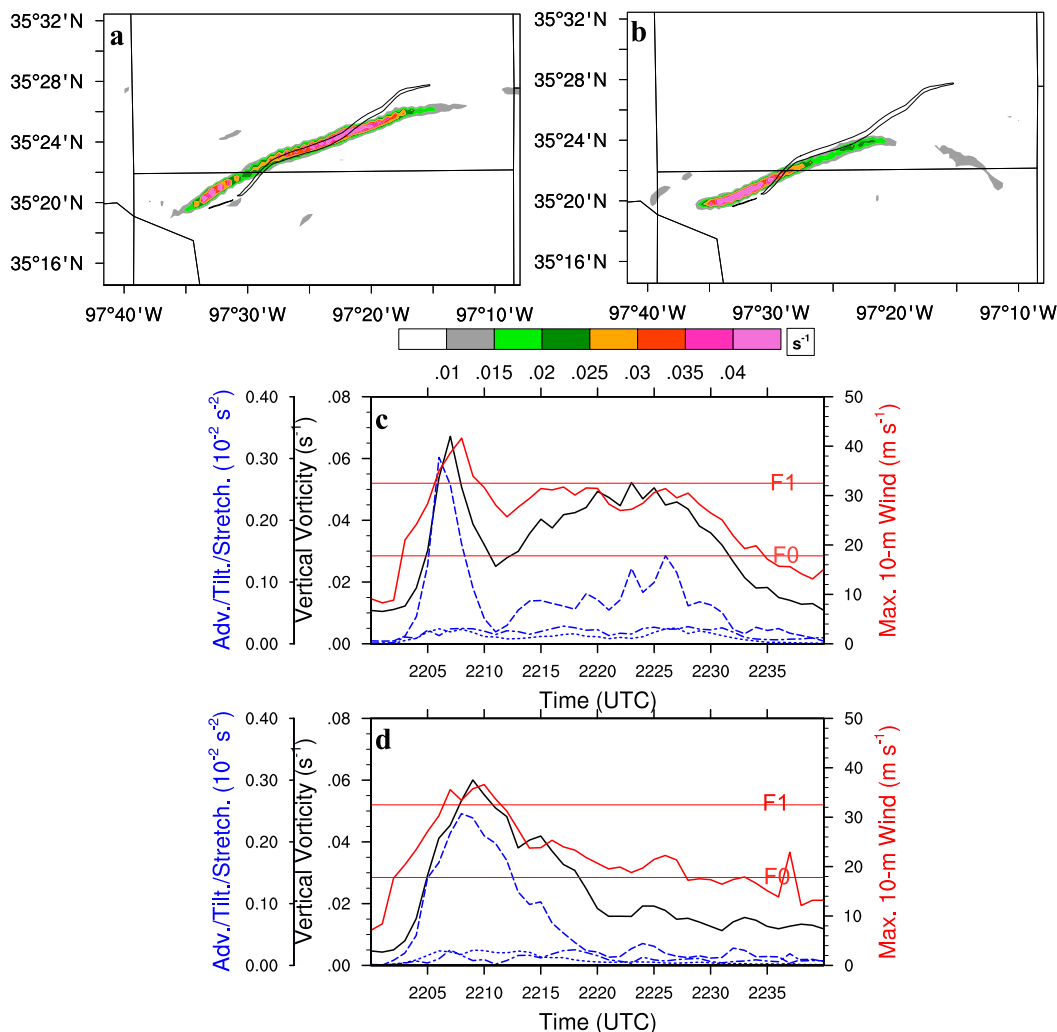
FIG. 12. Evolution of the near-surface vertical vorticity associated with the simulated TLVs from (a) Exp-DR and (b) Exp-SCR. The overlaid squiggly line in each panel is the NWS-observed tornado damage tracks during 2204–2238 UTC as in Fig. 1. The time series of maximum 10-m wind speed (red), vertical surface vorticity (black), and maxima of the horizontal advection (dotted–dashed), tilting (dotted), and stretching (dashed) terms in the vertical vorticity equation within a 1-km horizontal distance of the peak surface vorticity from (c) Exp-DR and (d) Exp-SCR. The two horizontal red lines in both figures indicate the magnitudes of F0 and F1 tornado intensities, respectively.

vorticity are presented for both experiments in Figs. 12c and 12d. The stretching term is remarkably greater than the tilting and advection terms at almost all forecast periods, especially during the periods with significant vortices. The vertical vorticity maxima most closely follow the maxima of the stretching term in both experiments, implying that the near-surface TLVs are intensified mostly through the stretching process. This result is consistent with the findings in previous studies (e.g., Klemp and Rotunno 1983; Wicker and Wilhelmson 1995; Noda and Niino 2010; Roberts et al. 2016; Rotunno et al. 2017) that the stretching (convergence) dominantly contributes to the latter stages of tornadogenesis and its persistence.

The variation of the vertical vorticity in relation to the variation of the low-level convergence is also validated in Fig. 13. Here the low-level convergence can be derived by the vertical gradient of vertical velocity below 1 km AGL in Figs. 13a and 13b. Exp-DR produces two periods of the persistent strong low-level convergence, 2203–2209 and 2213–2226 UTC (Fig. 13a), while only one period of low-level convergence from 2202 to 2216 UTC is found in Exp-SCR (Fig. 13b). In both experiments, the strong low-level vertical vorticity is accompanied by the enhanced low-level convergence (Figs. 13a,b) and strongest positive stretching near the surface (Figs. 13c,d). As the downdraft begins to
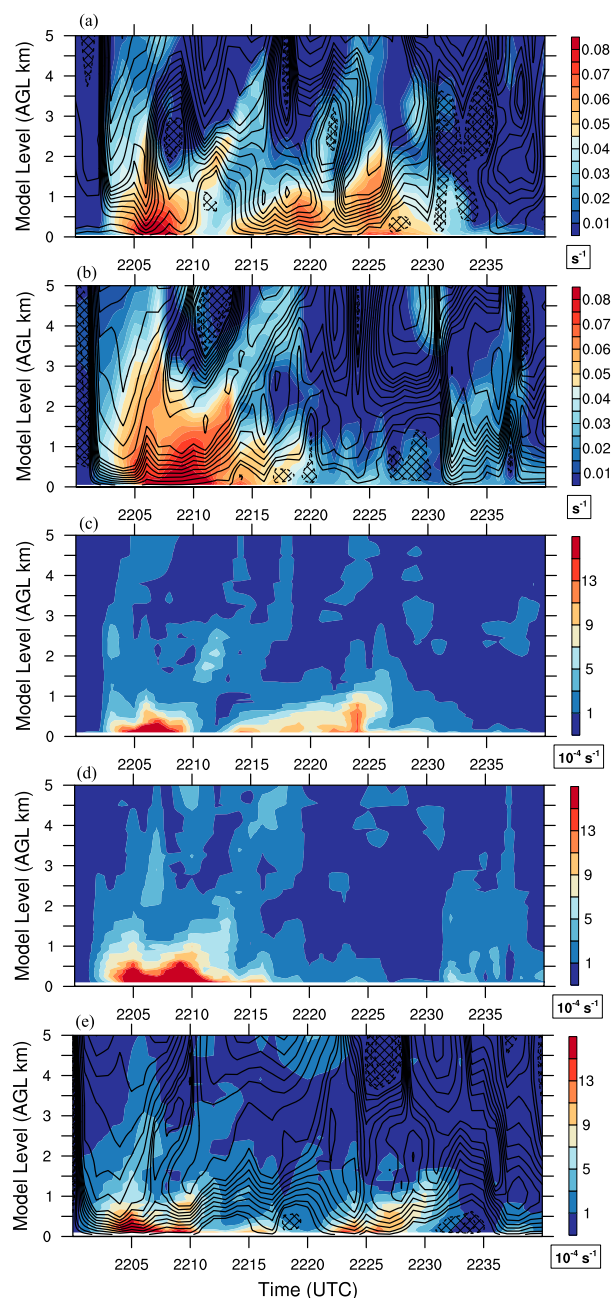
FIG. 13. Peak vertical vorticity (colors; s^{-1}) and mean vertical motion (contours from -3 to $9\,m\,s^{-1}$ at $1\,m\,s^{-1}$ interval and 9 to $30\,m\,s^{-1}$ at $3\,m\,s^{-1}$ interval; $m\,s^{-1}$) within the surface maximum vertical vorticity as a function of height and time for (a) Exp-DR and (b) Exp-SCR during 2200–2240 UTC. Solid contours (pattern shading) represent upward (downward) motion. Stretching of vertical vorticity (colors; s^{-2}) at the surface vorticity maximum for (c) Exp-DR, (d) Exp-SCR, and (e) Exp-T during 2200–2240 UTC. Mean vertical motion within the surface maximum vertical vorticity for Exp-T is overlaid in (e).

develop near the surface and shifts into the vorticity maxima, the weakening convergence or the strengthening divergence below 1-km AGL coincides with the reduced stretching and the weakened near-surface vertical vorticity. This can be seen, for example, from 2209 to 2213 UTC and after 2230 UTC in Exp-DR (Figs. 13a,c), and after 2219 UTC in Exp-SCR (Figs. 13b,d). However, some weak low-level downdrafts during the periods of 2226–2230 UTC in Exp-DR (Fig. 13a) and 2216–2219 UTC in Exp-SCR (Fig. 13b) are found to be aligned with large vertical vorticity and strong stretching near the ground. These weak low-level downdrafts during these periods are also directly under the greatly reduced vertical vorticity above 1 km AGL. Note that the vertical velocity in Fig. 13 is an average over an area within the 1 km radius around the maximum surface vorticity center. Updrafts and downdrafts coexist in the averaging area below 1 km AGL, although the downdraft is slightly stronger. These downdrafts are speculated to be induced by the low-level vertical vorticity that is stronger than that aloft (Klemp and Rotunno 1983). This downdraft-inducing process is the so-called "vortex valve effect" (Lewellen 1971; Lemon et al. 1975; Trapp 2000). These downdrafts can enhance the nearby updraft and the associated near-surface convergence and vorticity as long as they are not strong enough to devastate the low-level rotations (Markowski et al. 2002; Marquis et al. 2016).

3) IMPACT OF VERTICAL ALIGNMENT OF LOW-LEVEL CONVERGENCE AND MIDLEVEL UPDRAFT ON THE TLV EVOLUTION

Prior studies found that a tornado can be maintained when the low-level convergence is located beneath the midlevel updraft (Dowell and Bluestein 2002); while the displacement of the TLV and its associated low-level convergence from the updraft aloft may lead to the demise of a tornado (Wakimoto and Martner 1992; Wicker and Wilhelmson 1995; Snook and Xue 2008; Marquis et al. 2012). Consistent with these prior studies, the significant vortices near the surface (Figs. 12c,d) are accompanied by strong low-level convergence and the updraft above 1 km AGL in both experiments (Figs. 13a,b). Starting from 2207 UTC, the weakening low-level vorticity in Exp-DR coincides with either the reduced updraft strength, the appearance of a downdraft above 1 km AGL, or the misalignment of the updraft core aloft with the TLV-related low-level convergence. After 2213 UTC, both the low-level convergence and the updraft aloft (e.g., 1–2 km AGL) are gradually enhanced. The vertical vorticity near the surface starts to increase accordingly in Exp-DR (Fig. 13a). These results are consistent with the weakening and reintensification of the surface vorticity core in

TABLE 2. List of the replaced analyzed fields in sensitivity experiments.

Expt	Fields to be replaced in the ICs
Exp-Hydro	Hydrometeor mixing ratios, including rainwater, snow, graupel, and ice mixing ratios
Exp-T	Potential temperature (θ)
Exp-UVW	Kinematic fields (u, v, and w)
Exp-UVWT	Potential temperature (θ) and kinematic fields (u, v, and w)

Exp-DR in Figs. 12a and 12c. Different from Exp-DR where the weakening midlevel updraft reaches down to 0.5 km AGL, in Exp-SCR such a weakening midlevel updraft or appearance of a downdraft starting at 2207 UTC primarily occurs above 3 km AGL and the structures below 3 km AGL are barely affected. Therefore, the low-level significant vortices persist until 2215 UTC in Exp-SCR (Fig. 12d). This result is also consistent with the surface vorticity variation of weakening without reintensification in Exp-SCR.

The comparisons between Exp-DR and Exp-SCR are briefly summarized as follows. Relative to Exp-SCR, Exp-DR performs closer to the observations in the timing of the intensity variation and in the duration of the predicted TLV tracks. These different performances are found to agree well with the differences between both experiments in the low-level convergence and its vertical placement with respect to the midlevel updraft. As these predicted differences are caused by the differences in initial conditions (ICs), the following section 4d provides qualitative explanations to understand how these differences in ICs can affect the subsequent TLV predictions from a physical process perspective.

d. Diagnosing impact of the SCR and DR EnVar analyses on the predicted TLV

According to the comparisons between Exp-SCR and Exp-DR in section 4a, their IC differences can be classified into three categories: the vertical distributions of hydrometeor mixing ratios, the coverage and size of RF cold pools, and the structure and strength of the updraft and downdraft. To isolate the impact of each difference on the subsequent TLV predictions, four additional sensitivity experiments are conducted, shown in Table 2.[3] To examine the impact of the differences in the vertical reflectivity distributions, Exp-Hydro is the same as Exp-SCR except the analyzed hydrometeors are replaced by that from Exp-DR at the analysis time valid at 2200 UTC

---

[3] None of the replacement experiments show an initial shock during the early stage of the model integration.

8 May 2003. Exp-UVW aims to identify the impact of the differences in the kinematic fields by substituting the analyzed kinematic fields in Exp-SCR with that from Exp-DR. Cold pool evolution can be affected by several factors (i.e., temperature and moisture fields) (James et al. 2010). Replacement of either the analyzed potential temperature or the analyzed water vapor mixing ratio from Exp-DR can enhance the analyzed cold pools in Exp-SCR. However, potential temperature is found to dominate (not shown). Exp-T is therefore used to examine the impact of the differences in the analyzed cold pools where the analyzed potential temperature in Exp-SCR is replaced with that in Exp-DR. The combined impact of the differences in both kinematic fields and cold pools is given for experiment Exp-UVWT through the replacement of both from Exp-DR. Through comparison with Exp-UVW, Exp-UVWT can also examine the impact of the differences in cold pools.

Figure 14 shows the simulated TLV tracks from the sensitivity experiments in Table 2. The simulated TLV tracks here are represented by the near-surface vertical vorticity with its value greater than $0.03 \, \text{s}^{-1}$ as in Fig. 12. Exp-Hydro closely resembles Exp-SCR for the TLV track from 2204 to 2218 UTC (Fig. 14a). Exp-Hydro slightly enhances the short-lived second TLV track persisting only for ~1 min. In contrast, Exp-T produces two TLV tracks. The first of these TLVs persists from 2204 to 2218 UTC similar to the single TLV in Exp-SCR and Exp-Hydro. The duration of the first is longer than the observed damage track in Fig. 1. The second TLV track appears and intensifies beginning at 2223 UTC. Its track is located about 3 km east-northeast of the first one and persists for 5 min (Fig. 14b). Experiments Exp-UVW (Fig. 14c) and Exp-UVWT (Fig. 14d) both have two TLV tracks, but with different timings of the intensity variation compared to Exp-T. In Exp-UVW and Exp-UVWT, their first TLV tracks are maintained during the period from 2205 to 2210 UTC with the second TLV tracks appearing around 2215 UTC, consistent with the timing of the intensity variation of TLV in Exp-DR. However, Exp-UVW produces a remarkably weaker and shorter-lived TLV track from 2215 to 2226 UTC than Exp-UVWT and Exp-DR. In contrast, the duration of the second TLV track from 2215 to 2233 UTC in Exp-UVWT is more similar to Exp-DR (2213–2232 UTC).

In summary, compared with the timing of the observed tornado damage tracks (Fig. 1), the duration of the first TLV track is too long in Exp-Hydro and Exp-T. Replacing the analyzed kinematic fields in Exp-UVW and Exp-UVWT, the timing of maturation, dissipation, and reintensification for the TLV agrees well with the observations. After replacing the analyzed potential temperature, the duration of the second TLV track in
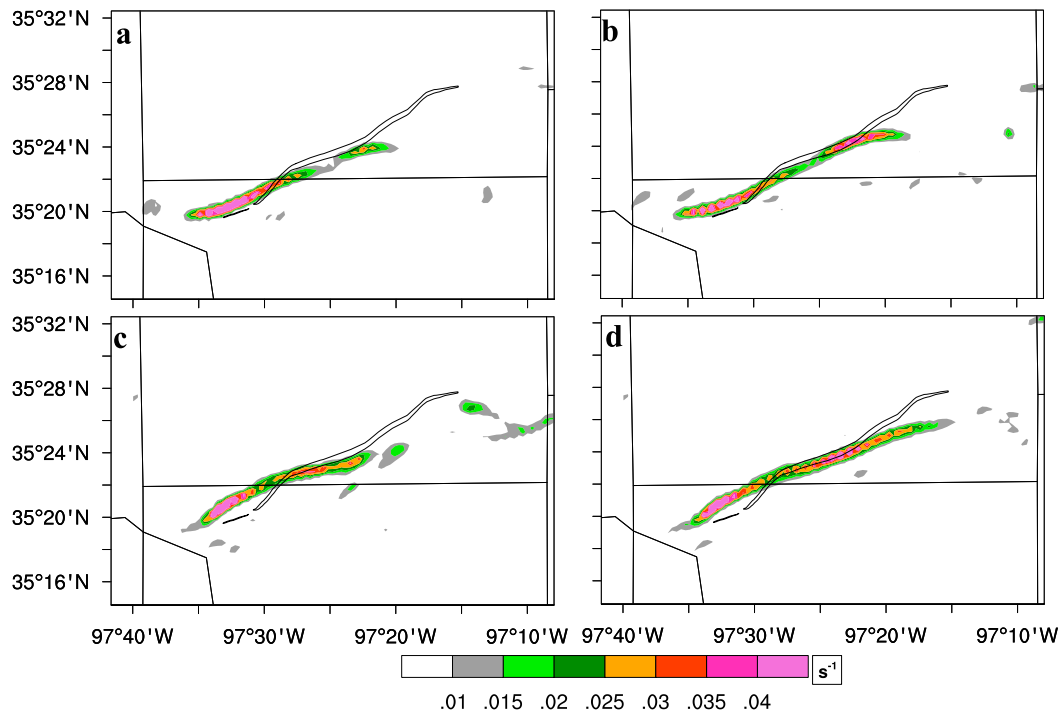
FIG. 14. As in Figs. 12a,b, but for (a) Exp-Hydro, (b) Exp-T, (c) Exp-UVW, and (d) Exp-UVWT in Table 1.

Exp-T and Exp-UVWT is extended compared to Exp-SCR and Exp-UVW, respectively. Replacing the hydrometeor mixing ratios in Exp-Hydro has only insignificant changes in the predicted TLV from Exp-SCR. Exp-Hydro becomes similar to Exp-SCR in less than 10 min (not shown). Together, these comparisons indicate that the analyzed kinematic variables in Exp-DR strongly affect the timing of intensity variation of the TLV, including the TLV's dissipation and reintensification; the duration of the second TLV track is associated with the analyzed potential temperature and the impact of the analyzed hydrometeor mixing ratios is negligible. The following process-based qualitative diagnostics facilitate a physical understanding of how the IC differences in the kinematic and potential temperature fields could impact the subsequent TLV evolutions. It is noted that this paper only intends to identify some plausible mechanisms that may be *consistent* with the differences in the evolution of the TLVs between Exp-SCR and Exp-DR. Other mechanisms may also be consistent and more robust analysis is required to adjudicate between them.

1) COLD POOL EVOLUTION DIFFERENCES

Numerous observational and idealized numerical studies (e.g., Leslie and Smith 1978; Markowski et al. 2002, 2003; Snook and Xue 2008; Lerach and Cotton 2012) found tornadogenesis significantly relies on the characteristics of cold pools. This section describes the major differences in

cold pool evolution and characteristics among Exp-SCR, Exp-T, and Exp-UVW. These differences are then used to explain the impact of analyzed kinematic fields and potential temperature on TLV predictions in sections 4d(2) and 4d(3). Relative to Exp-SCR (Figs. 11i–p), Exp-T consistently produces at least 3 K stronger cold pools in both RF and FF regions (Figs. 11q–x) during 2200–2220 UTC. The cold pool strength between Exp-SCR and Exp-UVW is comparable (Figs. 11y–af). However, the RF cold pool in Exp-UVW more quickly expands east-northeastward than both its FF cold pool and the RF cold pool in Exp-SCR, particularly at the earlier forecast periods (i.e., before 2220 UTC; Figs. 11y–ac). The FF broadening cold pools in the later forecast periods are comparable in strength among all experiments (Fig. 11). Such broadening cold pool is induced by a broadening downdraft commonly found in early studies (e.g., Lemon and Doswell 1979; Wicker and Wilhelmson 1995; Marquis et al. 2016). It is, however, noted that the timing of the FF broadening downdraft is different among different experiments. Specifically, the broadening downdraft in Exp-UVW and Exp-SCR occurs earlier[4] between 2220 and

---

[4] The occurrence of the broadening downdraft is indicated by the enhanced and enlarged cold pool, where the equivalent potential temperature near the low-level mesocyclone lower than 336 K is used to define the enhancing cold pool.
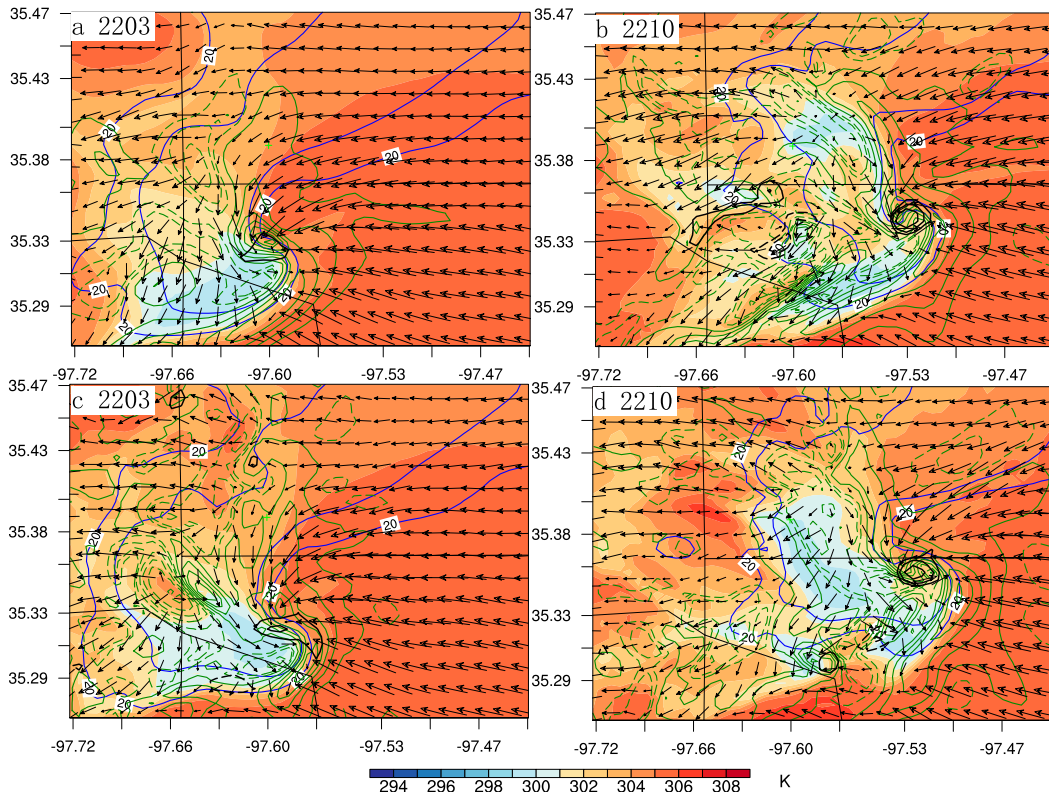
FIG. 15. Equivalent potential temperature (colors; K), vertical vorticity (thin black contours from 0.01 to 0.08 s^{-1} at intervals 0.01 s^{-1}; s^{-1}), and reflectivity (blue contours at 20 and 40 dBZ) near the ground and vertical velocity (green contours from -10 to 14 m s^{-1} at intervals 2 m s^{-1}; m s^{-1}) at 500 m AGL. These fields are valid at (a),(c) 2203 and (b),(d) 2210 UTC for (a),(b) Exp-SCR and (c),(d) Exp-UVW.

2225 UTC (Figs. 11m,n,ac,ad), followed by Exp-T between 2225 and 2230 UTC (Figs. 11v,x).

2) IMPACT OF ANALYZED KINEMATIC FIELDS

The analyzed kinematic variables here are represented by the vertical velocity at 2 km AGL in Fig. 7. Relative to Exp-SCR, Exp-DR has a stronger RF downdraft and a broadly stronger updraft, especially over the RF area. Such a stronger RF downdraft in Exp-DR persists during the subsequent forecast (Figs. 16a–c vs Figs. 17a–c). Replacement of the kinematic fields in Exp-UVW can also maintain a similar stronger RF downdraft during the forecast period (Fig. 15). The low-level RF downdraft maxima in Exp-UVW are 6 and 4 m s^{-1} greater than that in Exp-SCR, respectively, at 2203 UTC (Figs. 15a,c) and at 2210 UTC (Figs. 15b,d). As discussed in section 4d(1), relative to Exp-SCR, this stronger downdraft is consistent with the stronger west-southwesterly RF cold pool outflow following the RFGF and therefore a faster east-northeastward movement of the RFGF in Exp-UVW (Figs. 10y–af and 15).

To understand the impact of the kinematic field differences, especially the downdraft differences on the timing of the intensity variation of TLV, comparisons of the storm and TLV structures between Exp-SCR and Exp-DR/Exp-UVW/Exp-UVWT are conducted during the stages of maturation, weakening, and reintensification for the TLV (e.g., 2206–2215 UTC). As Exp-DR and Exp-UVW/Exp-UVWT have similar structures during the period for the first TLV track, the storm and TLV structures in Exp-DR at all developmental stages are shown in Fig. 16 and compared with Exp-SCR in Fig. 17. The bands of updraft cores at 2 km AGL in Figs. 16a–c and 17a–c indicate the spatial locations of the convergence and the GFs near the surface. During the period of 2206–2215 UTC, due to the strong west-southwesterly RF cold pool outflow surge, the RFGF moves east-northeastward more rapidly than the left-flank convergence boundary (LFCB). The updraft cores aloft therefore are gradually separated in Exp-DR (Fig. 16). At 2206 UTC, the southern midlevel updraft core is ~4 km east of the northern one (Fig. 16a); after 9 min, the two updraft cores are separated by more than 9 km at 2215 UTC (Fig. 16c). Along with the separating updraft cores, the meso-cyclone (illustrated with green dots in Figs. 16a–c or
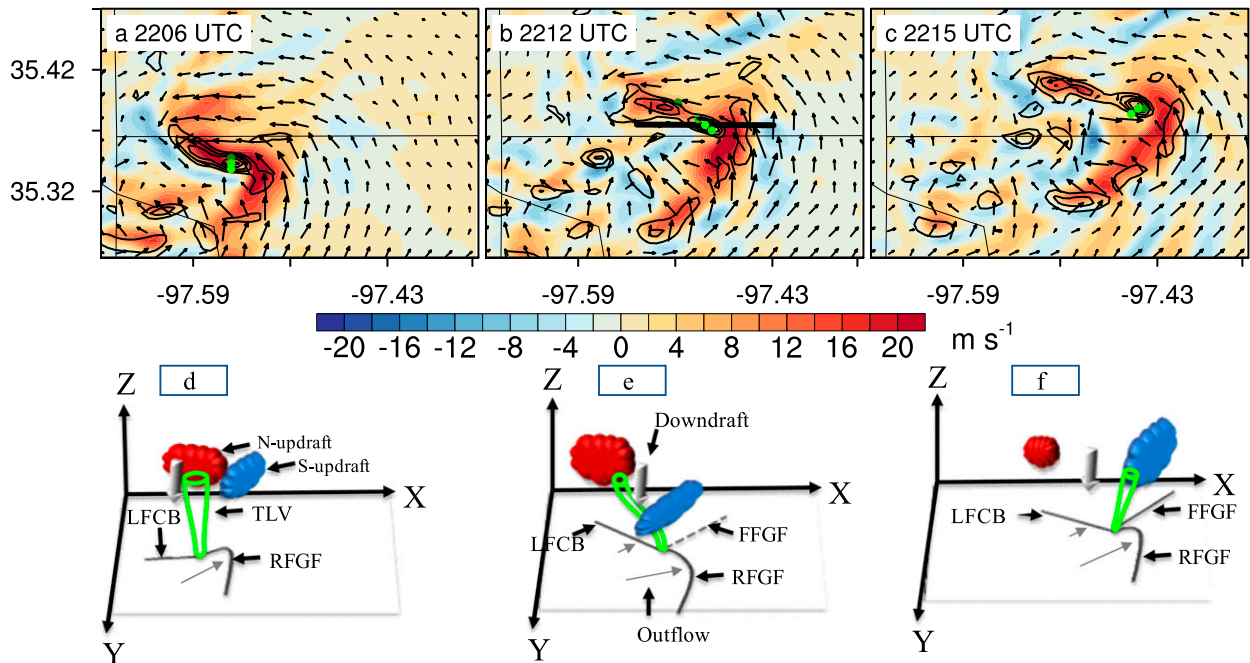
FIG. 16. The vertical velocity (colors; m s^{-1}) and cyclonic vorticity (contours from 0.01 to 0.04 s^{-1} at 0.01 s^{-1} intervals; s^{-1}) at 2 km AGL in the forecasts valid at (a) 2206, (b) 2212, and (c) 2215 UTC for Exp-DR. The green dots in (a)–(c) represent the maximum cyclonic vorticity at 0.1, 1, 2.5, and 4 km AGL, respectively. (d)–(f) Schematic diagram of the TLV evolution processes from 2206 to 2215 UTC is illustrated. Green columns refer to the structure of TLV, gray thick vectors indicate the downdraft trailing the updrafts, and N-updraft (red bulk) and S-updraft (blue bulk) represents the northern and southern midlevel updraft cores, respectively. The intensity of TLV is indicated schematically with the thickness of green column. In the x–y horizontal sections, the gray thin vectors indicate the rear-flank (RF) downdraft outflow and its strength is indicated schematically with the length of vectors; near-surface gust fronts are traced with bold black lines. The left-flank convergence boundary (LFCB), rear-flank gust front (RFGF), and forward-flank gust front (FFGF) are annotated with gray thick lines. The straight black line in (b) indicates the location of the vertical cross section in Fig. 18.

green columns in Figs. 16d–f) is increasingly tilted from the ground to the upper levels (e.g., 4 km AGL) in a southeast–northwest orientation during 2206–2212 UTC. Between 2212 and 2215 UTC, it gradually becomes vertically stacked. On the contrary, Exp-SCR fails to capture such a process. It produces a much weaker west-southwesterly RF cold pool outflow associated with its weaker downdraft. As a result, unlike Exp-DR, the two updraft cores of Exp-SCR are moving at a similar speed without being gradually separated during 2206–2215 UTC (Figs. 17a–f). The mesocyclone is vertically stacked throughout this period.

For Exp-DR, the near-surface mesocyclone (light green dot in Fig. 16b) travels east-northeastward faster than the northern midlevel updraft cores, consistent with the strong west-southwesterly RF cold pool outflow at low levels from 2206 to 2211 UTC. The vertical misalignment between the surface rotation center motion and the northern updraft core aloft tends to undercut or inhibit the vorticity stretching (Brooks et al. 1993; Markowski et al. 2003) required for the enhancement of the TLV. This is consistent with the decreasing near-surface stretching in Figs. 12c and 13c

during 2208–2211 UTC. After 4 min, the near-surface vorticity is gradually reintensified, consistent with the low-level mesocyclone that becomes increasingly vertically aligned with the southern midlevel updraft core (Figs. 16c,f). For Exp-SCR, due to the weaker RF cold pool outflow associated with the weaker downdraft, the similar tilt of the vertical alignment between the surface rotation center and the updraft core aloft is not found. Therefore the near-surface vorticity could be maintained for an unrealistically longer time than the first TLV track in Exp-DR.

We notice both the vorticity and the stretching near the surface have an abrupt decrease occurring at ~2208 UTC but an increase with a much slower rate from 2211 UTC for Exp-DR (Figs. 13a,c). The decrease is associated with the tilt of the mesocyclone as discussed in Fig. 16b. However, the relatively slow increase may be caused by the low-level (i.e., below 1 km AGL) downdraft surrounding the near-surface rotation center in Fig. 13a, despite the rotation center being located beneath the updraft core along the southern RFGF at 2211 UTC (Fig. 16b). To investigate this low-level air descent, a vertical cross section of
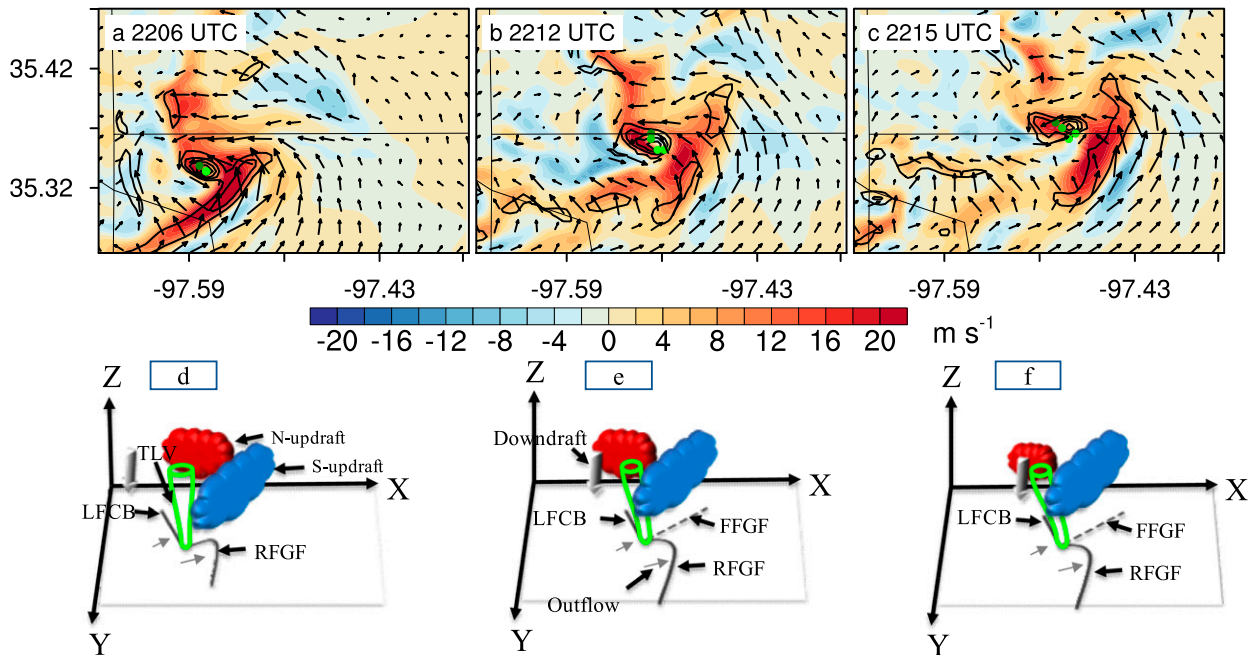
FIG. 17. As in Fig. 16, but for Exp-SCR.

vertical velocity and vertical vorticity along the black line in Fig. 16b is shown in Fig. 18. The low-level rotation core is located west of the updraft maximum along the RFGF and ~3 km away from the convergence center near the ground. A descent below 1 km AGL within the low-level rotation almost aligns along its rotation axis. This may be caused by the stronger low-level vorticity overlaid with a weaker rotation aloft, which could induce a downward pressure gradient force (Klemp and Rotunno 1983). The weaker rotation aloft is present within the updraft core along the RFGF and may be produced with cyclonic vorticity and anticyclonic vorticity straddling the vertical velocity maxima above 2 km AGL. This typically occurs in an environment where the horizontal vorticity is crosswise [Fig. 7 of Davies-Jones (1984)].

3) IMPACT OF ANALYZED POTENTIAL TEMPERATURE

Comparisons of the simulated TLV tracks between Exp-SCR (Exp-UVW) and Exp-T (Exp-UVWT) suggest that the duration of the second TLV track could be affected by the analyzed potential temperature (θ; Fig. 12b vs Figs. 14b,c vs Fig. 14d). As discussed in section 4d(1), the replacement of analyzed θ can enhance the RF and FF cold pools in the subsequent forecasts. This corresponds to the strengthened low-level latent cooling rate relative to Exp-SCR (Fig. 11). These stronger cold pools could be maintained during the forecast period through more hydrometeor loading and evaporation.

The longevity of the second TLV track in Exp-T can be attributed to the following three factors. First, relative to Exp-SCR, the stronger cold pool in Exp-T can cause greater cold pool outflow (Markowski et al. 2008), which favors the enhancement of the low-level convergence surrounding the low-level mesocyclone during 2222–2228 UTC, as shown in Fig. 13e. Meanwhile, low-level stretching is also increased, which is consistent with the discussions in section 4c. According to earlier studies (e.g., Klemp and Rotunno 1983; Wicker and Wilhelmson 1995; Noda and Niino 2010; Roberts et al. 2016; Rotunno et al. 2017), the increased stretching can be associated with the
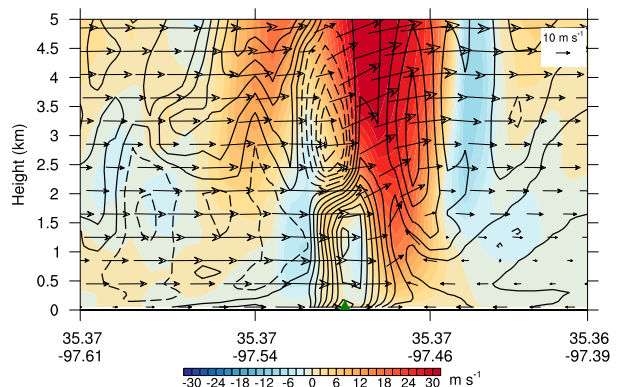

FIG. 18. Vertical cross sections of vertical velocity (colors; m s^{-1}) and vertical vorticity (contours from -0.04 to 0.08 s^{-1} at 0.005 s^{-1} intervals; s^{-1}) along the black think line in Fig. 16b for the forecast of Exp-DR valid at 2211 UTC. The green triangle indicates the location of low-level rotation core.

enhanced second TLV track in Exp-T and Exp-UVWT. Second, as discussed in section 4d(1), the broadening downdraft near the low-level mesocyclone in Exp-T occurs later than Exp-SCR (Fig. 11). Therefore, the surface rotation center could be taken over by the large-scale downdraft in Exp-T later than in Exp-SCR, contributing to the longevity of TLV in Exp-T. A similar trend is also found in the comparison between Exp-UVW and Exp-UVWT. Third, the stronger RF cold pool in Exp-UVWT and Exp-T can provide more baroclinically induced horizontal vorticity (Markowski et al. 2008), which may facilitate the TLV development (Klemp and Rotunno 1983).

It is noted that previous studies (e.g., Snook and Xue 2008; Lerach et al. 2008; Dawson et al. 2015) found a simulated longer-lived tornado is associated with weaker cold pools rather than stronger ones. The result in this paper is not inconsistent with these studies, as the stronger cold pool in this study with an equivalent potential temperature deficit of ~8 K (i.e., Figs. 10f,v) is comparable with their weaker cold pool. Our result also suggests too weak of the cold pool like that in Exp-SCR may not favor a longer-lived tornado. These results are consistent with Markowski et al. (2008).

5. Summary and discussion

Plenty of previous studies adopted proxy forecasts of tornadoes inferred from strong mid- and low-level rotations, mostly in simulations with a 1–3 km grid spacing. However, it has been demonstrated that the existence and strength of such rotations are not reliable indicators for tornado occurrence. An explicit forecast of tornadoes or tornado-like vortices (TLVs) provides a more accurate representation of the existence of tornadoes in model simulations. Given the small size of tornado vortices, it is clear that a subkilometer grid spacing is essential to resolve the finescale properties of tornadoes or TLVs. A few prior studies have attempted to predict the tornadoes or TLVs at a subkilometer grid spacing. However, these subkilometer TLV predictions are initialized by downscaling from a coarse-resolution analysis with grid spacings ≥1 km in most of these studies. To address the impact of subkilometer versus kilometer grid spacing on ICs and the subsequent TLV predictions, two experiments are designed. In the first experiment, an efficient dual-resolution (DR) approach is extended within the GSI-based EnVar framework to directly produce a 500-m analysis by ingesting a 2-km ensemble with a 500-m control first guess. The second experiment adopts a single-coarse-resolution (SCR) EnVar where the ICs are produced at a 2-km grid spacing, ingesting a 2-km ensemble. The subsequent high-resolution TLV predictions are conducted at a 500-m grid spacing for both experiments.

The impact of subkilometer versus kilometer grid spacing ICs are examined on the 8 May 2003 Oklahoma City tornadic supercell storm with simulations produced by the WRF-ARW Model. Radar observations including reflectivity and radial velocity are assimilated every 5 min starting at 2100 UTC 8 May 2003 for a total period of 1 h. Direct assimilation of reflectivity using reflectivity as a state variable is employed (Wang and Wang 2017). A 45-member ensemble at 2-km grid spacing is used in both GSI-based DR and SCR EnVar systems and their initial ensemble is downscaled from mesoscale ensemble analyses. The 2-km control analysis for SCR and the 500-m control analysis for DR are, respectively, provided to recenter the 2-km EnKF ensemble analyses.

Comparisons of the ICs between the two experiments show that DR produces a stronger and more widespread RF cold pool, more intense downdraft and updraft fields with finer-scale features, and increased reflectivity at high altitudes relative to SCR. Further diagnostics for each DA cycle and from a DA algorithm perspective indicate that these differences are an accumulated impact of integrating the higher-resolution analyses, updating the higher-resolution background, and propagating the ensemble perturbations along the trajectory of a higher-resolution grid in DR than in SCR. It is found that DR can better capture the storm evolution than SCR by maintaining a well-defined hook echo and strong radial velocity couplet for more than 30 min, which is closer to the reality than SCR. Observations from two METAR stations suggest that the stronger cold pool and its evolution in DR are more realistic than in SCR. The differences in ICs lead to remarkably different TLV tracks in the subsequent forecasts. The TLV tracks in DR fit better with the observations with two TLV tracks. Specifically, the DR TLVs are more consistent with the observed tornado damage tracks in both the timing of the intensity variation and the duration of the TLV. On the contrary, in the SCR experiment, only one TLV track persists for ~20 min, which is unrealistically longer than the first observed tornado track. Detailed diagnostics suggest that these differences in the simulated TLV tracks agree well with the differences in the low-level convergence and its vertical placement with the midlevel updraft between DR and SCR.

The diverse evolutions of the simulated TLVs are caused by the different features in the ICs between DR and SCR. The IC differences include three categories: vertical distributions of the hydrometeor mixing ratios, the cold pool represented by the potential temperature, and the downdraft and updraft with finescale features. To isolate the impact of each difference on the TLV predictions, four additional sensitivity experiments are conducted. In these experiments, the TLV predictions

are initialized from the ICs in which the analyzed variables in SCR are individually replaced by those in DR. Qualitative diagnostics of these experiments are performed to assist physical understanding of the differences in the TLV predictions. These results are summarized as follows.

1) The analyzed downdraft and updraft fields largely influence the timing of the variation of the TLV intensity, including the weakening and reintensification for the TLV. Compared to SCR, the stronger RF downdraft in DR produces a stronger RF outflow. Therefore, the RF cold pool accompanying the RFGF expands east-northeastward faster than the FF cold pool. The near-surface rotation center then travels east-northeastward faster than the northern updraft core aloft due to the greater RF outflow. Such tilt results in TLV weakening. As the low-level mesocyclone is increasingly vertically stacked with the southern midlevel updraft core, the near-surface vorticity is gradually reintensified. For SCR, the weaker RF cold pool outflow, consistent with the weaker RF downdraft, leads to little or no tilt between the near-surface mesocyclone and the northern updraft core aloft. Therefore, the near-surface vorticity is maintained for an unrealistically long time.

2) The duration of the second TLV track is associated with potential temperature differences in the ICs. Compared to SCR, the stronger RF cold pool produced in the DR analysis persists during the entire forecast period, most likely through the increased precipitation loading and evaporation. Intensification of near-surface vorticity is consistent with the enhanced stretching due to the increased convergence and (or) more horizontal baroclinic vorticity supply associated with the colder cold pool. In addition, the analyzed potential temperature from DR favors the delay of the broadening large-scale downdraft near the surface mesocyclone. Therefore the TLV in the experiments with the analyzed potential temperature from DR is longer lived.

3) The experiment replacing the analyzed hydrometeor mixing ratios from DR essentially resembles SCR. It is found that the distribution of hydrometeor mixing ratios consistent with the kinematic fields is adjusted back to be similar to SCR in less than 10 min. Therefore, the impact of isolated hydrometeor mixing ratios is negligible.

This study utilizes a 500-m horizontal grid spacing to predict the TLV to understand the impact of subkilometer versus kilometer grid spacing analyses on the subkilometer TLV predictions. However, tornado-scale circulations cannot be fully resolved in our simulations with a 500-m grid spacing. Explicit simulations of tornadoes require at least 100-m grid spacing, even 50 m as shown by Xue et al. (2014). With this finer resolution, it is possible to more explicitly reveal the tornado-scale circulations. Given the consistency between the horizontal and vertical resolutions (Lindzen and Fox-Rabinovitz 1989), the impact of the vertical resolution on the TLV predictions also needs to be considered in future work. In addition, the sensitivity experiments indicate the evolution of the modeled TLV can be significantly affected by physical variations of the cold pool, etc., which strongly relies on the choice of physical parameterization schemes, especially microphysics and planetary boundary layer schemes. Future studies are required to investigate the performances of different schemes on the TLV predictions.

REFERENCES

Adlerman, E. J., and K. K. Droegemeier, 2002: The sensitivity of numerically simulated cyclic mesocyclogenesis to variations in model physical and computational parameters. *Mon. Wea. Rev.*, **130**, 2671–2691, https://doi.org/10.1175/1520-0493(2002)130<2671:TSONSC>2.0.CO;2.

Brooks, H. E., C. A. Doswell, and R. Davies-Jones, 1993: Environmental helicity and the maintenance and evolution of low-level mesocyclones. *The Tornado: Its Structure, Dynamics, Prediction, and Hazards, Geophys. Monogr.*, Vol. 79, Amer. Geophys. Union, 97–104.

Burgess, D. W., 2004: High resolution analyses of the 8 May 2003 Oklahoma City storm, Part I: Storm structure and evolution from radar data. *22nd Conf. on Severe Local Storms*, Hyannis, MA, Amer. Meteor. Soc., 12.4, http://ams.confex.com/ams/pdfpapers/81939.pdf.

——, D. C. Dowell, L. J. Wicker, and A. Witt, 2005: Detailed comparison of observed and modeled tornadogenesis. *32nd Conf. on Radar Meteorology*, Albuquerque, NM, Amer. Meteor. Soc., 10R.4, http://ams.confex.com/ams/pdfpapers/97377.pdf.

Chen, F., and J. Dudhia, 2001: Coupling an advanced land surface–hydrology model with the Penn State–NCAR MM5 modeling system. Part I: Model implementation and sensitivity. *Mon. Wea. Rev.*, **129**, 569–585, https://doi.org/10.1175/1520-0493(2001)129<0569:CAALSH>2.0.CO;2.

Davies-Jones, R., 1984: Streamwise vorticity: The origin of updraft rotation in supercell storms. *J. Atmos. Sci.*, **41**, 2991–3006, https://doi.org/10.1175/1520-0469(1984)041<2991:SVTOOU>2.0.CO;2.

Dawson, D. T., M. Xue, J. A. Milbrandt, and M. K. Yau, 2010: Comparison of evaporation and cold pool development between single-moment and multimoment bulk microphysics schemes in idealized simulations of tornadic thunderstorms. *Mon. Wea. Rev.*, **138**, 1152–1171, https://doi.org/10.1175/2009MWR2956.1.

——, L. J. Wicker, E. R. Mansell, and R. L. Tanamachi, 2012: Impact of the environmental low-level wind profile on ensemble forecasts of the 4 May 2007 Greensburg, Kansas, tornadic storm and associated mesocyclones. *Mon. Wea. Rev.*, **140**, 696–716, https://doi.org/10.1175/MWR-D-11-00008.1.

——, M. Xue, J. A. Milbrandt, and A. Shapiro, 2015: Sensitivity of real-data simulations of the 3 May 1999 Oklahoma City tornadic supercell and associated tornadoes to multimoment microphysics. Part I: Storm- and tornado-scale numerical forecasts. *Mon. Wea. Rev.*, **143**, 2241–2265, https://doi.org/10.1175/MWR-D-14-00279.1.

Dowell, D. C., and H. B. Bluestein, 2002: The 8 June 1995 McLean, Texas, storm. Part II: Cyclic tornado formation, maintenance, and dissipation. *Mon. Wea. Rev.*, **130**, 2649–2670, https://doi.org/10.1175/1520-0493(2002)130<2649:TJMTSP>2.0.CO;2.

——, and L. J. Wicker, 2009: Additive noise for storm-scale ensemble data assimilation. *J. Atmos. Oceanic Technol.*, **26**, 911–927, https://doi.org/10.1175/2008JTECHA1156.1.

——, F. Zhang, L. J. Wicker, C. Snyder, and N. A. Crook, 2004: Wind and temperature retrievals in the 17 May 1981 Arcadia, Oklahoma, supercell: Ensemble Kalman filter experiments. *Mon. Wea. Rev.*, **132**, 1982–2005, https://doi.org/10.1175/1520-0493(2004)132<1982:WATRIT>2.0.CO;2.

——, L. J. Wicker, and C. Snyder, 2011: Ensemble Kalman filter assimilation of radar observations of the 8 May 2003 Oklahoma City supercell: Influences of reflectivity observations on storm-scale analyses. *Mon. Wea. Rev.*, **139**, 272–294, https://doi.org/10.1175/2010MWR3438.1.

Fiori, E., A. Parodi, and F. Siccardi, 2010: Turbulence closure parameterization and grid spacing effects in simulated supercell storms. *J. Atmos. Sci.*, **67**, 3870–3890, https://doi.org/10.1175/2010JAS3359.1.

Gao, J., and M. Xue, 2008: An efficient dual-resolution approach for ensemble data assimilation and tests with simulated Doppler radar data. *Mon. Wea. Rev.*, **136**, 945–963, https://doi.org/10.1175/2007MWR2120.1.

Hanley, K. E., A. I. Barrett, and H. W. Lean, 2016: Simulating the 20 May 2013 Moore, Oklahoma tornado with a 100-metre grid-length NWP model. *Atmos. Sci. Lett.*, **17**, 453–461, https://doi.org/10.1002/asl.678.

Hu, M., and M. Xue, 2007: Impact of configurations of rapid intermittent assimilation of WSR-88D radar data for the 8 May 2003 Oklahoma city tornadic thunderstorm case. *Mon. Wea. Rev.*, **135**, 507–525, https://doi.org/10.1175/MWR3313.1.

Iacono, M. J., J. S. Delamere, E. J. Mlawer, M. W. Shepard, S. A. Clough, and W. D. Collins, 2008: Radiative forcing by long-lived greenhouse gases: Calculations with the AER radiative transfer models. *J. Geophys. Res.*, **113**, D13103, https://doi.org/10.1029/2008JD009944.

James, R. P., and P. M. Markowski, 2010: A numerical investigation of the effects of dry air aloft on deep convection. *Mon. Wea. Rev.*, **138**, 140–161, https://doi.org/10.1175/2009MWR3018.1.

Janjić, Z. I., 1990: The step-mountain coordinate: Physical package. *Mon. Wea. Rev.*, **118**, 1429–1443, https://doi.org/10.1175/1520-0493(1990)118<1429:TSMCPP>2.0.CO;2.

——, 1994: The step-mountain eta coordinate model: Further developments of the convection, viscous sublayer, and turbulence closure schemes. *Mon. Wea. Rev.*, **122**, 927–945, https://doi.org/10.1175/1520-0493(1994)122<0927:TSMECM>2.0.CO;2.

——, 2002: Nonsingular implementation of the Mellor–Yamada level 2.5 scheme in the NCEP Meso model. NCEP Office Note 437, 61 pp., http://www.emc.ncep.noaa.gov/officenotes/newernotes/on437.pdf.

Jung, Y., M. Xue, and M. Tong, 2012: Ensemble Kalman filter analyses of the 29–30 May 2004 Oklahoma tornadic thunderstorm using one- and two-moment bulk microphysics schemes, with verification against polarimetric data. *Mon. Wea. Rev.*, **140**, 1457–1475, https://doi.org/10.1175/MWR-D-11-00032.1.

Kay, J., and X. Wang, 2020: A multiresolution ensemble hybrid 4DEnVar for global numerical prediction. *Mon. Wea. Rev.*, **148**, 825–847, https://doi.org/10.1175/MWR-D-19-0002.1.

Klemp, J. B., and R. Rotunno, 1983: A study of the tornadic region within a supercell thunderstorm. *J. Atmos. Sci.*, **40**, 359–377, https://doi.org/10.1175/1520-0469(1983)040<0359:ASOTTR>2.0.CO;2.

Lakshmanan, V., T. Smith, G. Stumpf, and K. Hondl, 2007: The Warning Decision Support System–Integrated Information. *Wea. Forecasting*, **22**, 596–612, https://doi.org/10.1175/WAF1009.1.

Lemon, L. R., and C. A. Doswell, 1979: Severe thunderstorm evolution and mesocyclone structure as related to tornadogenesis. *Mon. Wea. Rev.*, **107**, 1184–1197, https://doi.org/10.1175/1520-0493(1979)107<1184:STEAMS>2.0.CO;2.

——, D. W. Burgess, and R. A. Brown, 1975: Tornado production and storm sustenance. Preprints, *Ninth Conf. on Severe Local Storms*, Norman, OK, Amer. Meteor. Soc., 100–104.

Lerach, D. G., and W. R. Cotton, 2012: Comparing aerosol and low-level moisture influences on supercell tornadogenesis: Three-dimensional idealized simulations. *J. Atmos. Sci.*, **69**, 969–987, https://doi.org/10.1175/JAS-D-11-043.1.

——, B. J. Gaudet, and W. R. Cotton, 2008: Idealized simulations of aerosol influences on tornadogenesis. *Geophys. Res. Lett.*, **35**, L23806, https://doi.org/10.1029/2008GL035617.

Leslie, L. M., and R. K. Smith, 1978: The effect of vertical stability on tornadogenesis. *J. Atmos. Sci.*, **35**, 1281–1288, https://doi.org/10.1175/1520-0469(1978)035<1281:TEOVSO>2.0.CO;2.

Lewellen, W. S., 1971: A review of confined vortex flows. NASA Contractor Rep. NASA CR-1772, 219 pp.

Lindzen, R. S., and M. Fox-Rabinovitz, 1989: Consistent vertical and horizontal resolution. *Mon. Wea. Rev.*, **117**, 2575–2583, https://doi.org/10.1175/1520-0493(1989)117<2575:CVAHR>2.0.CO;2.

Lu, X., X. Wang, M. Tong, and V. Tallapragada, 2017: GSI-based, continuously cycled, dual-resolution hybrid ensemble–variational data assimilation system for HWRF: System description and experiments with Edouard (2014). *Mon. Wea. Rev.*, **145**, 4877–4898, https://doi.org/10.1175/MWR-D-17-0068.1.

Markowski, P. M., J. M. Straka, and E. N. Rasmussen, 2002: Direct surface thermodynamic observations within the rear-flank downdrafts of nontornadic and tornadic supercells. *Mon. Wea. Rev.*, **130**, 1692–1721, https://doi.org/10.1175/1520-0493(2002)130<1692:DSTOWT>2.0.CO;2.

——, ——, and ——, 2003: Tornadogenesis resulting from the transport of circulation by a downdraft: Idealized numerical simulations. *J. Atmos. Sci.*, **60**, 795–823, https://doi.org/10.1175/1520-0469(2003)060<0795:TRFTTO>2.0.CO;2.

——, Y. Richardson, E. Rasmussen, J. Straka, R. Davies-Jones, and R. J. Trapp, 2008: Vortex lines within low-level mesocyclones obtained from pseudo-dual-Doppler radar observations. *Mon. Wea. Rev.*, **136**, 3513–3535, https://doi.org/10.1175/2008MWR2315.1.

——, ——, M. Majcen, J. Marquis, and J. Wurman, 2011: Characteristics of the wind field in a trip of nontornadic low-level mesocyclones observed by the Doppler on Wheels radars. *Electron. J. Severe Storms Meteor.*, **6** (3), https://www.ejssm.org/ojs/index.php/ejssm/article/viewArticle/75.

——, and Coauthors, 2012: The pretornadic phase of the Goshen County, Wyoming, supercell of 5 June 2009 intercepted by VORTEX2. Part II: Intensification of low-level rotation. *Mon. Wea. Rev.*, **140**, 2916–2938, https://doi.org/10.1175/MWR-D-11-00337.1.

Marquis, J., Y. Richardson, P. Markowski, D. Dowell, and J. Wurman, 2012: Tornado maintenance investigated with high-resolution dual-Doppler and EnKF analysis. *Mon. Wea. Rev.*, **140**, 3–27, https://doi.org/10.1175/MWR-D-11-00025.1.

——, ——, ——, ——, ——, K. Kosiba, P. Robinson, and G. Romine, 2014: An investigation of the Goshen County, Wyoming, tornadic supercell of 5 June 2009 using EnKF assimilation of mobile mesonet and radar observations collected during VORTEX2. Part I: Experiment design and verification of the EnKF analyses. *Mon. Wea. Rev.*, **142**, 530–554, https://doi.org/10.1175/MWR-D-13-00007.1.

——, ——, ——, J. Wurman, K. Kosiba, and P. Robinson, 2016: An investigation of the Goshen County, Wyoming, tornadic supercell of 5 June 2009 using EnKF assimilation of mobile mesonet and radar observations collected during VORTEX2. Part II: Mesocylone-scale processes affecting tornado formation, maintenance, and decay. *Mon. Wea. Rev.*, **144**, 3441–3463, https://doi.org/10.1175/MWR-D-15-0411.1.

Mashiko, W., H. Niino, and T. Kato, 2009: Numerical simulation of tornadogenesis in an outer-rainband minisupercell of Typhoon Shanshan on 17 September 2006. *Mon. Wea. Rev.*, **137**, 4238–4260, https://doi.org/10.1175/2009MWR2959.1.

Mellor, G. L., and T. Yamada, 1982: Development of a turbulence closure model for geophysical fluid problems. *Rev. Geophys. Space Phys.*, **20**, 851–875, https://doi.org/10.1029/RG020i004p00851.

NCDC, 2003: *Storm Data*. Vol. 45, No. 5.

Noda, A., and H. Niino, 2003: Critical grid size for simulating convective storms: A case study of the Del City supercell storm. *Geophys. Res. Lett.*, **30**, 1844, https://doi.org/10.1029/2003GL017498.

Noda, A. T., and H. Niino, 2010: A numerical investigation of a supercell tornado: Genesis and vorticity budget. *J. Meteor. Soc. Japan*, **88**, 135–159.

Potvin, C. K., E. M. Murillo, M. L. Flora, and D. M. Wheatley, 2017: Sensitivity of supercell simulations to initial-condition resolution. *J. Atmos. Sci.*, **74**, 5–26, https://doi.org/10.1175/JAS-D-16-0098.1.

Rainwater, S., and B. Hunt, 2013: Mixed resolution ensemble data assimilation. *Mon. Wea. Rev.*, **141**, 3007–3021, https://doi.org/10.1175/MWR-D-12-00234.1.

Roberts, B., M. Xue, A. D. Schenkman, and D. T. Dawson, 2016: The role of surface drag in tornadogenesis within an idealized supercell simulation. *J. Atmos. Sci.*, **73**, 3371–3395, https://doi.org/10.1175/JAS-D-15-0332.1.

Romine, G. S., D. W. Burgess, and R. B. Wilhelmson, 2008: A dual-polarization-radar-based assessment of the 8 May 2003 Oklahoma City area tornadic supercell. *Mon. Wea. Rev.*, **136**, 2849–2870, https://doi.org/10.1175/2008MWR2330.1.

Rotunno, R., P. M. Markowski, and G. H. Bryan, 2017: "Near ground" vertical vorticity in supercell thunderstorm models. *J. Atmos. Sci.*, **74**, 1757–1766, https://doi.org/10.1175/JAS-D-16-0288.1.

Schenkman, A. D., M. Xue, and A. Shapiro, 2012: Tornadogenesis in a simulated mesovortex within a mesoscale convective system. *J. Atmos. Sci.*, **69**, 3372–3390, https://doi.org/10.1175/JAS-D-12-038.1.

——, ——, and M. Hu, 2014: Tornadogenesis in a high-resolution simulation of the 8 May 2003 Oklahoma City supercell. *J. Atmos. Sci.*, **71**, 130–154, https://doi.org/10.1175/JAS-D-13-073.1.

Schwartz, C. S., 2016: Improving large-domain convection-allowing forecasts with high-resolution analyses and ensemble data assimilation. *Mon. Wea. Rev.*, **144**, 1777–1803, https://doi.org/10.1175/MWR-D-15-0286.1.

——, Z. Liu, and X. Y. Huang, 2015: Sensitivity of limited-area hybrid variational-ensemble analyses and forecasts to ensemble perturbation resolution. *Mon. Wea. Rev.*, **143**, 3454–3477, https://doi.org/10.1175/MWR-D-14-00259.1.

Seko, H., M. Kunii, S. Yokota, T. Tsuyuki, and T. Miyoshi, 2015: Ensemble experiments using a nested LETKF system to reproduce intense vortices associated with tornadoes of 6 May 2012 in Japan. *Prog. Earth Planet. Sci.*, **2**, 42, https://doi.org/10.1186/s40645-015-0072-3.

Snook, N., and M. Xue, 2008: Effects of microphysical drop size distribution on tornadogenesis in supercell thunderstorms. *Geophys. Res. Lett.*, **35**, L24803, https://doi.org/10.1029/2008GL035866.

Sobash, R. A., G. S. Romine, C. S. Schwartz, D. J. Gagne, and M. L. Weisman, 2016: Explicit forecasts of low-level rotation from convection-allowing models for next-day tornado prediction. *Wea. Forecasting*, **31**, 1591–1614, https://doi.org/10.1175/WAF-D-16-0073.1.

Tanamachi, R. L., L. J. Wicker, D. C. Dowell, H. B. Bluestein, D. T. Dawson II, and M. Xue, 2013: EnKF assimilation of high-resolution, mobile Doppler radar data of the 4 May 2007 Greensburg, Kansas, supercell into a numerical cloud model. *Mon. Wea. Rev.*, **141**, 625–648, https://doi.org/10.1175/MWR-D-12-00099.1.

Thompson, G., P. R. Field, R. M. Rasmussen, and W. R. Hall, 2008: Explicit forecasts of winter precipitation using an improved bulk microphysics scheme. Part II: Implementation of a new snow parameterization. *Mon. Wea. Rev.*, **136**, 5095–5115, https://doi.org/10.1175/2008MWR2387.1.

Thompson, T. E., L. J. Wicker, X. Wang, and C. Potvin, 2015: A comparison between the local ensemble transform Kalman filter and the ensemble square root filter for the assimilation of radar data in convective-scale models. *Quart. J. Roy. Meteor. Soc.*, **141**, 1163–1176, https://doi.org/10.1002/qj.2423.

Trapp, R. J., 1999: Observations of nontornadic low-level mesocyclones and attendant tornadogenesis failure during VORTEX. *Mon. Wea. Rev.*, **127**, 1693–1705, https://doi.org/10.1175/1520-0493(1999)127<1693:OONLLM>2.0.CO;2.

——, 2000: A clarification of vortex breakdown and tornadogenesis. *Mon. Wea. Rev.*, **128**, 888–895, https://doi.org/10.1175/1520-0493(2000)128<0888:ACOVBA>2.0.CO;2.

Wakimoto, R. M., and B. E. Martner, 1992: Observations of a Colorado tornado. Part II: Combined photgrammetric and Doppler radar analysis. *Mon. Wea. Rev.*, **120**, 522–543, https://doi.org/10.1175/1520-0493(1992)120<0522:OOACTP>2.0.CO;2.

Wang, X., 2010: Incorporating ensemble covariance in the Gridpoint Statistical Interpolation (GSI) variational minimization: A mathematical framework. *Mon. Wea. Rev.*, **138**, 2990–2995, https://doi.org/10.1175/2010MWR3245.1.

——, D. Parrish, D. Kleist, and J. S. Whitaker, 2013: GSI 3DVar-based ensemble–variational hybrid data assimilation for NCEP Global Forecast System: Single-resolution experiments. *Mon. Wea. Rev.*, **141**, 4098–4117, https://doi.org/10.1175/MWR-D-12-00141.1.

Wang, Y., and X. Wang, 2017: Direct assimilation of radar reflectivity without tangent linear and adjoint of the nonlinear observation operator in the GSI-based EnVar system: Methodology and experiment with the 8 May 2003 Oklahoma City tornadic supercell. *Mon. Wea. Rev.*, **145**, 1447–1471, https://doi.org/10.1175/MWR-D-16-0231.1.

Whitaker, J. S., and T. M. Hamill, 2002: Ensemble data assimilation without perturbed observations. *Mon. Wea. Rev.*, **130**, 1913–1924, https://doi.org/10.1175/1520-0493(2002)130<1913:EDAWPO>2.0.CO;2.

——, and ——, 2012: Evaluating methods to account for system errors in ensemble data assimilation. *Mon. Wea. Rev.*, **140**, 3078–3089, https://doi.org/10.1175/MWR-D-11-00276.1.

——, ——, X. Wei, Y. Song, and Z. Toth, 2008: Ensemble data assimilation with the NCEP Global Forecast System. *Mon. Wea. Rev.*, **136**, 463–482, https://doi.org/10.1175/2007MWR2018.1.

Wicker, L. J., and R. B. Wilhelmson, 1995: Simulation and analysis of tornado development and decay within a three-dimensional supercell thunderstorm. *J. Atmos. Sci.*, **52**, 2675–2703, https://doi.org/10.1175/1520-0469(1995)052<2675:SAAOTD>2.0.CO;2.

Wurman, J., and C. R. Alexander, 2004: Scales of motion in tornadoes, what radars cannot see, what scale circulation is a tornado. Preprints, *22nd Conf. on Severe Local Storms,* Hyannis, MA, Amer. Meteor. Soc., P11.6, https://ams.confex.com/ams/pdfpapers/82353.pdf.

——, and K. Kosiba, 2013: Finescale radar observations of tornado and mesocyclone structures. *Wea. Forecasting*, **28**, 1157–1174, https://doi.org/10.1175/WAF-D-12-00127.1.

Xue, M., M. Hu, and A. D. Schenkman, 2014: Numerical prediction of the 8 May 2003 Oklahoma City tornadic supercell and embedded tornado using ARPS with the assimilation of WSR-88D data. *Wea. Forecasting*, **29**, 39–62, https://doi.org/10.1175/WAF-D-13-00029.1.

Yussouf, N., E. R. Mansell, L. J. Wicker, D. M. Wheatley, and D. J. Stensrud, 2013: The ensemble Kalman filter analyses and forecasts of the 8 May 2003 Oklahoma City tornadic supercell storm using single- and double-moment microphysics schemes. *Mon. Wea. Rev.*, **141**, 3388–3412, https://doi.org/10.1175/MWR-D-12-00237.1.